Journal of Bio- and Tribo-Corrosion (2023) 9:65
https://doi.org/10.1007/s40735-023-00783-4

Tribocorrosion of Additively Manufactured (AM-ed) Metallic Biomaterials in Hip Implants : Review on Methodology and Post Treatments

Mahmoud Naim[1,2] · Akram Alhussein[1,3] · Mahdi Chemkhi[1,2]

Received: 18 February 2023 / Revised: 24 May 2023 / Accepted: 29 June 2023 / Published online: 25 July 2023

Abstract
Additive manufacturing (AM) is an original manufacturing technique in which a part can be constructed layer by layer. The AM techniques help in constructing intricate structures that serve the proper functioning of the biomedical metallic hip implant. The latter is present in a biological aggressive environment and is prone to various dynamic stresses. Thus, the dominant wear mechanism in the metallic hip implant is tribocorrosion. During tribocorrosion, the interaction between various corrosion and wear mechanisms takes place. Certain protocols are followed to properly investigate the tribocorrosion mechanism and they are: ASTMG119 and UNE112086. An enormous number of studies were done on the tribocorrosion of conventionally processed metallic biomaterials. Nonetheless, a limited number of studies pedantically assess the tribocorrosion of AM-ed metallic biomaterials. In this review, the available protocols to investigate the tribocorrosion of metallic biomaterials are elaborated. Moreover, the state of art of the tribocorrosion of metallic AM-ed biomaterials deployed in biomedical hip implants is spanned. Finally, the potential post-treatments applied to ameliorate the tribocorrosion resistance of AM-ed metallic biomaterials utilized in hip implants are classified and discussed.

Keywords Tribocorrosion · Hip implant · Additive manufacturing · Post treatments

1 Introduction

Additive manufacturing (AM) has been recently evolving as a feasible alternative to subtractive manufacturing methods. In AM methods, the part is constructed layer by layer. The material extrusion (ME) fused deposition modeling (FDM) technique is the commonly used AM method and it is classically utilized to fabricate polymer parts. For metallic materials, the AM processes can be classified as direct or indirect metallic AM techniques [1]. In the direct AM processes, an energy source is employed to locally melt the powder material and build the work piece layer-wise. Nevertheless, in the indirect metallic AM methods such as metallic FDM, a filament that is highly filled with metallic powder is deposited to create the part layer by layer. After that, the print is washed in a debinding solution to partially remove the soluble polymer. Finally, the part is sintered in a furnace to achieve a quasi-fully dense metallic part. The metallic AM methods are utilized in various aeronautical [2, 3], space mobility [4], nuclear power [3], and biomedical applications [5] (e.g.hip implant). Metallic AM is considered as a promising manufacturing technique for various biomedical applications, where it is employed in virtual surgical planning and in the manufacturing of drug releasing implants. Moreover, it is used for the fabrication of biomedical parts such as dental [6] and surgical equipment [7], and orthotic and prosthetic devices [8]. The latter are customized based on the dimensions of the patient's treated organ [9]. Therefore, the AM techniques can play a pivotal role in manufacturing customized intricate biomedical implants at relatively low cost. The metallic AM processes can manipulate various bio-materials such as Ti [10], Zr [11]-based bulk metallic glasses, Ti6Al4V alloy [9], Ti27.5Nb alloy [12], Ti6Al7Nb

✉ Akram Alhussein
akram.alhussein@utt.fr

1 UR LASMIS, University of Technology of Troyes, 12 rue Marie Curie, 10000 Troyes, France

2 EPF Graduate School of Engineering, 2 Rue Fernand Sastre, 10000 Troyes, France

3 UR LASMIS, University of Technology of Troyes, Technological pole of South Champagne, 26 rue Lavoisier, 52800 Nogent, France

alloy, Ti24Nb4Zr alloy [13], Co-Cr alloys [14], shape-memory NiTi alloys [15], 316L stainless steel [16] and 17-4PH stainless steel [17].

1.1 Mechanical Requirements of the Metallic Biomaterial in a Hip Implant Application

The material deployed in biomedical hip implants must have an elastic modulus (E) that is relatively close to the E of the bone. The bone is constituted of an outer cortical bone shell ($E = 20$ GPa) that surrounds a spongy material ($E = 0.5$ GPa) [18]. The E of the bio-compatible metals (e.g. $E_{Ti6Al4V} = 116$ GPa & $E_{316LSS} = 193$ GPa [19]) is relatively higher than that of the bone. The discrepancy in the E between the hosting bone and the hip implant somehow impedes the transfer of stresses to the adjoining bone (Fig. 1a). This mechanism is named as "stress shielding" [18]. Wolffs law states:"the bone subjected to stress will regenerate and the bone that is not subjected to stress will atrophy" [20]. Therefore, if the stresses are not sufficiently transported to the bone, the bone undergo osteoporosis. During the latter, the bone atrophy and its density decrease. Thus, the risk of periprosthetic fracture is present [21]. The stress shielding causes bone resorption [22] which takes place via osteolysis. The latter is correlated with the aseptic loosening of the implant [23]. The aseptic loosening corresponds to the failure of the prosthetic implant in the absence of infections or mechanical actions [24]. Even though decreasing the gradient of E between the hip prosthesis and the bone minimizes the stress shielding effect, the proximal interfacial stresses augment. Consequently, the contact between the hip implant and the bone deteriorates due to the micro-motion and debonding [25]. The stress shielding problem and the loosening of the implant are resolved by deploying implants of specific scaffold structure. The latter may decrease the E of the hip implant to be closer to that of the bone and consequently, the stress shielding effect is alleviated. Moreover, the bone grows into the lattice structure to improve the osseointegration (Fig. 1b) [26–28]. The density (ρ) of the bone outer shell is about 1.99 g/cm^3 which is lower than that of the bio-compatible metallic materials for e.g. Ti ($\rho = 4.43$ g/cm^3) [18]. The prosthetic hip implant must also have a high yield stress (σ_y) to sustain the human body weight imposed on it. The hip prosthesis is also subjected to various dynamic forces especially when the patient is in motion. Thus, it is indispensable to fabricate a hip prosthesis with a high endurance limit to avoid any undesirable prospective surgical intervention. The fatigue life of a hip implant is mainly affected by the applied dynamic stresses, the porosity content, the manufacturing residual stresses, and the implant roughness. The porosities act as stress-rising sites at which crack initiation commences. Moreover, the manufacturing tensile residual stresses help in inducing crack propagation, however, the compressive ones tend to impede the crack propagation. The surface roughness may also impact the crack initiation mechanism that may starts in the vicinity of the surface. Residual stresses are generated in the hip implant after successive bone-implant interactions that yield to plastic deformation. This may reduce the lifetime of the hip implant. Furthermore, these residual stresses also trigger various thermodynamic potentials in the aggressive environment [29]. The prosthesis is present in an in-vivo aggressive environment that contains oxygen, chloride, protein, hydroxide and various anions and cations [30]. In such an environment, the hip implant is subjected to corrosion.

The hip implant is present in a highly aggressive medium that prone it to corrosion and is concurrently subjected to

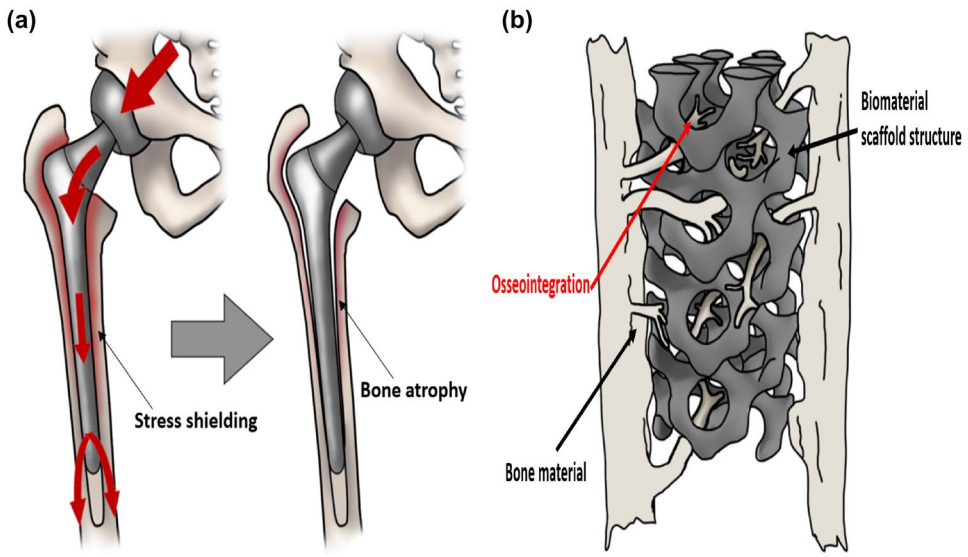

Fig. 1 **a** The stress shielding that yields bone atrophy and **b** the osseointegration of a hip implant with an intricate scaffold structure [31–33]

distinct dynamic stresses, specifically, at its junctions and at its interconnections with the bone (Fig. 2). Therefore, the implant is predominantly prone to tribocorrosion at the interfaces and junctions specified in Fig. 2. Generally, the hip implant is composed of various parts and they are the femoral stem, the femoral neck, the femoral head, and an acetabular cup (Fig. 2). The number of junctions in a hip implant is depicted by its type (e.g. monolithic or modular). In modular implants, in addition to the junction between the head and the neck and the interface between the head and the cup, another junction is present between the permutable neck and the stem. The interchangeable neck enables the independent modification of the implant offset and length. This offers versatility for the surgeon during the operation and in the primary revisions [34]. At the interconnection between the implant and the bone and at the junctions and interfaces in the implant, several types of tribocorrosion mechanisms can take place such as fretting corrosion and sliding-corrosion (Fig. 2).

Tribocorrosion is a wear mechanism that involves the interaction of corrosion with other wear mechanisms (i.e. abrasion, fretting, solid particle erosion, cavitation erosion, and adhesion and fatigue wear). Biological solutions (e.g. proteins) may play a role in the tribocorrosion mechanism [35–38]. There are several types of tribocorrosion mechanisms and they are classified based on the tribological and corrosion wear mechanisms that are taking place. The tribocorrosion wear can be a two body wear mechanism or may involve a third body that is incorporated in the tribological system. Tribocorrosion results in wear debris that may induce implant loosening and various biological reactions [39].To study the tribocorrosion of the metallic parts in aggressive environments distinct aspects of the physical problem must be considered such as the applied stresses, the tribological system (two body or three body), the surface chemistry, the microstructure (e.g. phases and grain boundary density) and the electrochemical activity of the surface. Therefore it is somehow an intricate mission to precisely comprehend the tribocorrosion wear mechanism that is taking place in the material. Thus, various experimental techniques are deployed to reach this goal.

Various works discussed the tribocorrosion mechanism aspects in conventionally manufactured biomaterials such as [40, 41]. In the literature, few review studies focus on the tribocorrosion of AM-ed metallic biomaterials [42]. Nonetheless, there exists no study that pedantically focuses on the current status of the tribocorrosion studies performed on AM-ed metallic biomaterials that are specifically used in a hip implant application. In this review, the tribocorrosion mechanisms that take place in the hip implant are studied with a focus on the fretting corrosion that takes place at the junctions and the interfaces of the implant. The available experimental protocols used to evaluate the in-vitro tribocorrosion of the materials are discussed. Moreover, the state of the art of tribocorrosion of the AM-ed metallic biomaterials utilized in a hip implant application is spanned. Furthermore, the existing post-treatments applied to ameliorate the tribocorrosion resistance of conventionally manufactured and AM-ed metallic biomaterials are classified and discussed.

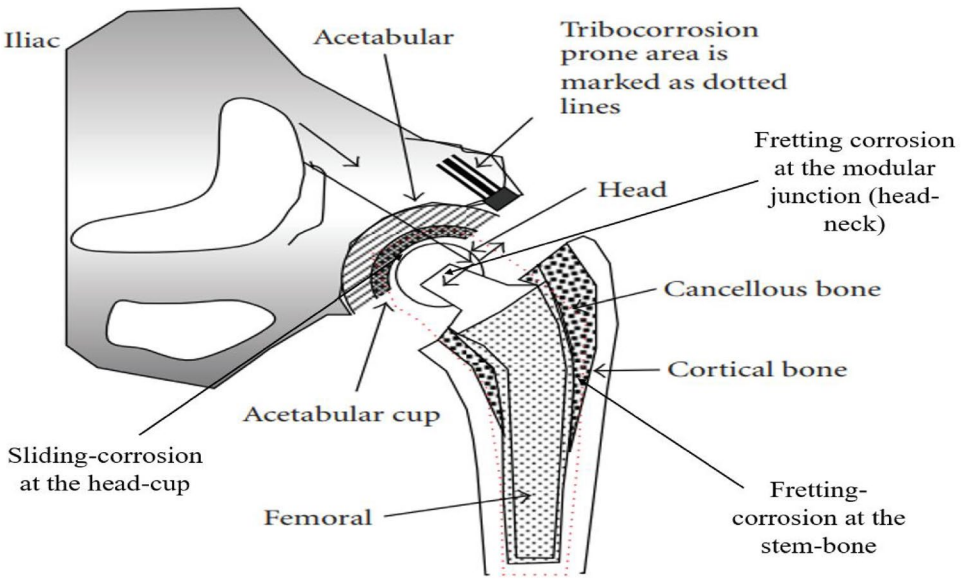

Fig. 2 The regions that are prone to tribocorrosion in the metal-on-metal hip implant (circumscribed with dots) [36, 43]

2 Tribocorrosion Wear Mechanism in a Metallic Hip Implant

The tribocorrosion wear mechanism mainly takes place at the interface between the implant stem and the bone, at the junctions in the implant, and at the interface between the head and the acetabular cup. Generally, in hip implants, fretting corrosion takes place. Fretting is a wear mechanism that is attributed to the micrometric oscillatory relative motion that takes place at the interfaces present in the implant and between the implant and the bone (Fig. 2). Depending on the magnitude of the reciprocation displacement, principle fretting regimes can be classified and they are full stick, mixed stick and slip, and gross slip. In the sticking regime, almost no wear debris is generated and no fatigue cracks are witnessed except at a very high number of cycles ($N \geq 10^6$) [44, 45]. In the mixed regime, crack initiation and propagation take place particularly at the annular boundary between the stick and the slip regions (i.e. fretting fatigue) [44, 45]. In the gross slip regime, a lot of wear particulates are produced and mainly fretting wear takes place [44]. The $\frac{\delta}{\delta_T}$ ratio is an index that can be utilized to figure out the present fretting regime (Fig. 3). In case $\delta > a$ then reciprocation sliding is taking place and not fretting [46] (Fig. 3).

The simultaneous actions of fretting and corrosion lead to the fretting corrosion tribocorrosion mechanism. In the literature, various studies discussed the fretting corrosion of materials used in hip implants. Costa et al. observed that the fretting behavior of porous Ti versus Ti6Al4V alloy in foetal bovine serum depends on the imposed load. Furthermore, it was found that the porous Ti morphology was not altered after the fretting corrosion test [49]. The reinforcement of plasma sintered Ti6Al4V with 10 $wt\%ZrO_2$ improves the fretting corrosion resistance in foetal bovine serum. Moreover, it was observed that the exhibited fretting regime is dependent on the imposed load. Furthermore, the ZrO_2 reinforcements may limit the release of the Ti, Al and V ions [50]. Fretting corrosion may take place at various locations in the hip implant (Fig. 2) and specifically at modular junctions.

The occurrence of fretting corrosion at the modular junction (i.e. the connection between the implant stem+neck and head) may lead to local inflammation in the biological environment surrounding the implant [51]. To ensure implant durability, it is important to manufacture a hip implant design with appropriate surface topography and material couples that yield a hip implant with high resistance to fretting corrosion. Feysi et al. meticulously examined the effect of the surface topography of necks present in the taper junctions of hip implants on the fretting corrosion at the junction and illustrated various scenarios for several material couples [51]. It was observed that the fretting corrosion is predominant at modular junctions in implants with Ti-6Al-4V femoral stem and CoCr femoral head and in the ones with CoCr femoral head and stem [52, 53]. Oladokun et al. evaluated the fretting corrosion behavior of CoCrMo–CoCrMo and CoCrMo–Ti6Al4V tribo-couples. A fatigue-dominant fretting mechanism and a wear-dominant fretting mechanism were observed for the CoCrMo–Ti6Al4V and the CoCrMo–CoCrMo fretting couples, respectively. Additionally, it is important to note the CoCrMo–Ti6Al4V fretting couple interface was prone to several localized corrosion mechanisms [47]. The fretting-corrosion behavior of CoCrMo alloy head/CoCrMo

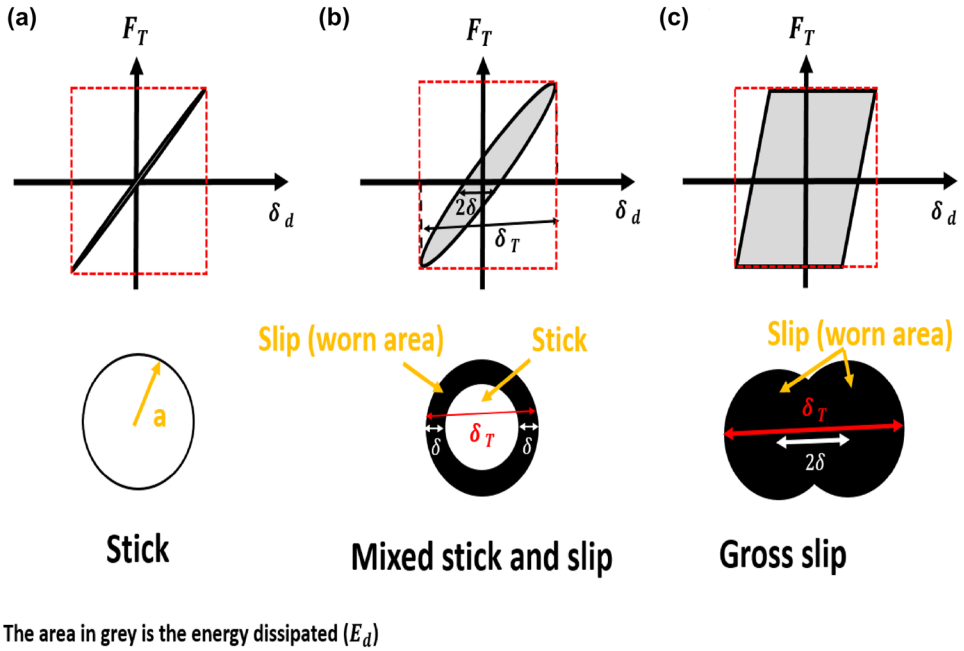

Fig. 3 The fretting wear mechanisms **a** sticking, **b** sticking and slipping and **c** gross slipping. F_T is the measured tangential force for a lateral solicitation, δ_d is the fretting amplitude, and δ is the displacement amplitude. The total energy is the area bounded by the red dotted lines. The enclosed area inside the fretting loops corresponds to the work done to shear the material surface (i.e. energy dissipated) [47, 48] (Color figure online)

alloy stem and ZrO_2 head/CoCrMo alloy stem were compared in fetal bovine serum. It was found that the ZrO_2 head/CoCrMo alloy stem somehow exhibits better resistance to fretting corrosion and almost less than or equal Cr and Co metal ion release to the electrolyte compared to the CoCrMo alloy/CoCrMo alloy couple [54]. There are several ways in which the metal ion release takes place and it can be either due to the dissociation of the passive layer, the wear, the corrosion of the bare material of the implant or to the the three modes together. For Ti6Al4V, the effect of Ti, Al and V release on the body is still controversial [50]. For CoCr alloys, on the long term, the release of the Co and Cr may lead to cancer even at currently accepted concentrations. Additionally, the Co ions can play a role in causing the death of macrophages and lymphocytes [55]. Co and Cr are also considered probable mutagenic metals. The in-vivo measurement of the metal ion release can be done via blood, urine or synovial fluid testing [56]. The choice of the test may depend on the metallic ion to be analyzed [57]. For in-vitro tests, the metallic ion levels can be measured via several methods such as atomic absorption spectroscopy, X-ray fluorescence spectrometry and inductively coupled plasma spectroscopy [58]. In addition to the metallic ions, the release of wear debris may have a biological detrimental effect on the body. Unlike the metal-on-polyethylene implants, the metal particles released in the metal-on-metal implants are nanometric and not micrometric. This can alleviate their reaction with the macrophages. Nonetheless, the nanoparticles particles and the ions released by such implants can be cytotoxic. The DNA harm attributed to metallic particles and ions may result in carcinogenesis [56]. Psuedotumors may also be formed due to the presence of an abundant amount of metallic wear particles. It must be noted that some patients may have a hypersensitivity to metals, which can yield an immunological reaction. Osteolysis has been also detected in metal-on-metal implants. Due to the complexity of the biological environment and the tribocorrosion wear mechanism, specific protocols, techniques and experimental conditions are deployed to extensively investigate the tribocorrosion wear mechanism.

3 Experimental Techniques and Protocols Followed to Evaluate the Tribocorrosion Behavior of Metallic Materials

3.1 The Experimental Methods Utilized to Study the Tribocorrosion of Metallic Biomaterials

The tribocorrosion performance of a material is usually analyzed using a combined tribometer-potentiostat setup (Fig. 4). To conduct a tribocorrosion test using the latter, a certain normal load and reciprocation frequency are specified. In the case of the tribocorrosion of a biomaterial deployed in a hip implant, a frequency of 3 Hz is applied, which is close to that of the average active joint movement in a normal human being [59]. After specifying the principle test parameters, the coefficient of friction (COF) and the open circuit potential (OCP) can be recorded. Moreover, potentiodynamic and potentiostatic polarization measurements can be achieved. Additionally, electrochemical impedance spectroscopy can be accomplished to pedantically understand the tribocorrosion mechanism.

3.1.1 OCP Measurement During Tribocorrosion of Metallic Biomaterials

The OCP, the corrosion potential or the rest potential is the potential (i.e. driving force) that depicts the propensity of a metal to undergo electrochemical oxidation in a corrosive environment. The OCP relies on the deployed experimental conditions (i.e. the dissolved oxygen content in the electrolyte and the concentration of certain anions in the aqueous solution, temperature and pH of the corrosive solution, and the superficial status of the material). At the OCP, the

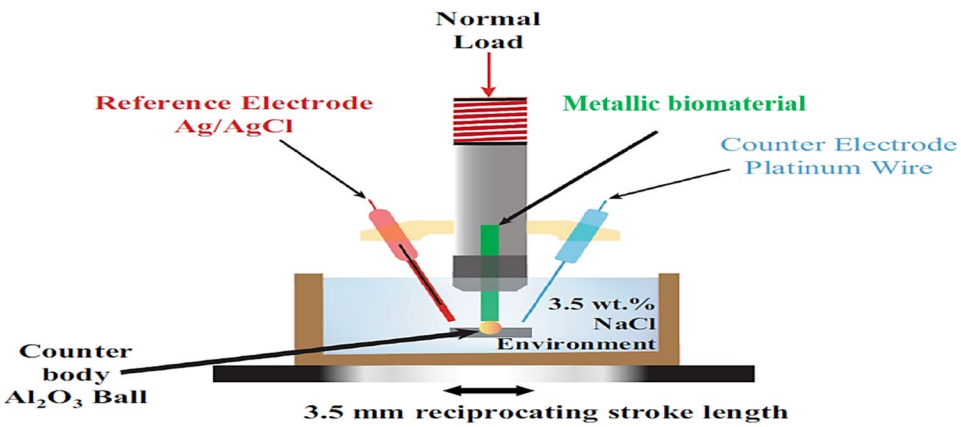

Fig. 4 The tribocorrosion test setup [35]

whole charge transfer between the metallic material and the electrolyte is in a state of equilibrium. Nonetheless, it is crucial to note that the redox reactions have distinct rates. This is attributed to the growth in the fraction of the electrochemically active regions and to the variations in the metal ambient environment. The changes in the OCP with time designate an alteration in the surface nature [60]. The decrease in the OCP toward more negative values indicates that the passive film is being destroyed and the increase of the OCP implies that the surface is undergoing passivation (Fig. 5). The protocol that is conventionally implemented to measure the OCP in a tribocorrosion experiment is achieved over three stages. In the first stage, the OCP is measured until stabilization is attained (Fig. 5). After that the wear test is conducted and concurrently the measured OCP drops and the COF is recorded. In the last stage, the wear test finishes and the OCP restabalizes [28, 59] (Fig. 5). It must be noted that after the tribocorrosion test, the wear rate which is defined as the volume of material lost per force and sliding distance can be computed.

3.1.2 Potentiodynamic and Potentiostatic Measurements

Potentiodynamic polarization measurements can be also achieved during the tribocorrosion test by monitoring the potential (i.e driving force) of the anodic and cathodic reactions, and concurrently, the net variation in the redox reaction rate (i.e. current) is recorded (Fig. 6). The potentiostat computes the current required for the system to accomplish the targeted augmentation in the potential or driving force. Potentiostatic experiments may also be done to track the variation of the corrosion current during the tribocorrosion experiment at specific potential [60]. In the potentiostatic measurements a certain potential is applied on the working electrode and the current is recorded.

3.1.3 Electrochemical Impedance Spectroscopy Analysis

Electrochemical impedance spectroscopy (EIS) measurements can be accomplished in the course of the tribocorrosion test as illustrated in Fig. 7 to meticulously understand the tribo-electrochemical mechanisms taking place.EIS is accomplished by sending a small AC sinusoidal excitation signal E_t (1-10mv) [63] that is shown below [64]:

$$E_t = E_0 \sin(wt) \tag{1}$$

where E_t is the potential at a certain time (t), E_0 is the signal amplitude and $w = 2\pi f$ is the radial frequency and f is the frequency. The response signal to the excitation is I_t which is the current at t, it has a certain frequency phase shift (ϕ) and it is represented by the equation below [64]:

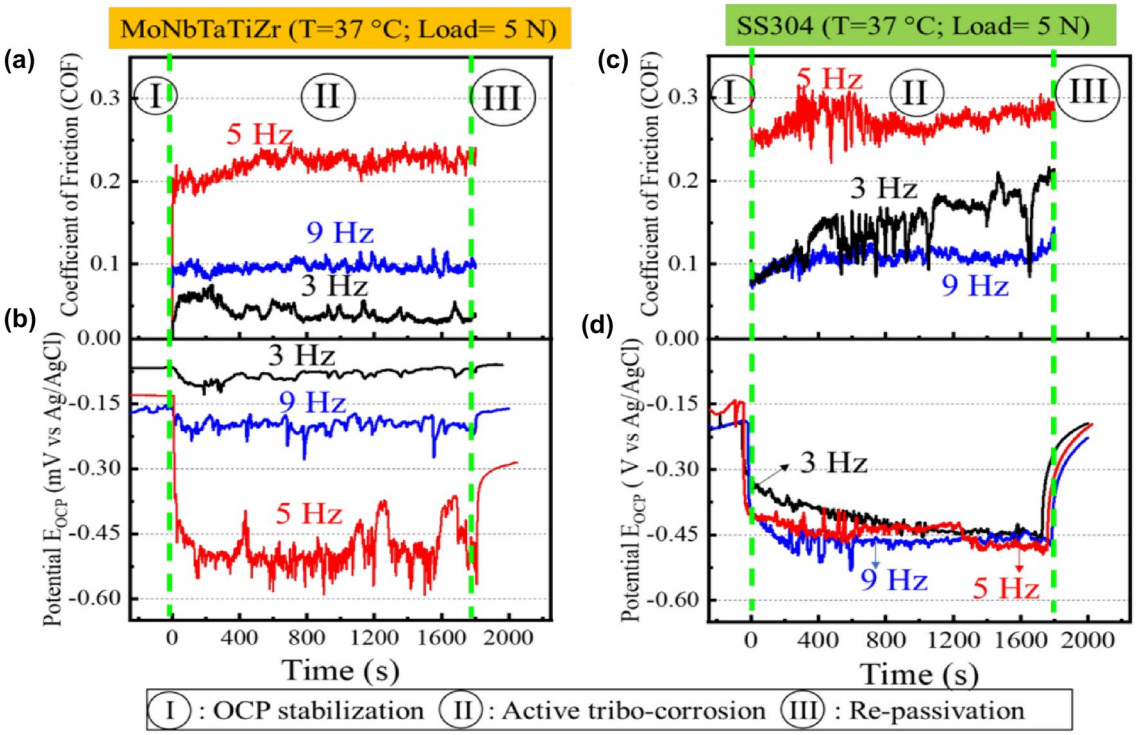

Fig. 5 The variation of the **a**, **c** COF and **b**, **d** OCP during the tribocorrosion test performed on MoNbTaTiZr and 304 stainless steel in simulated body fluid at 37 °C at distinct reciprocation frequencies (i.e. 3 Hz, 5 Hz,and 15 Hz) [59]

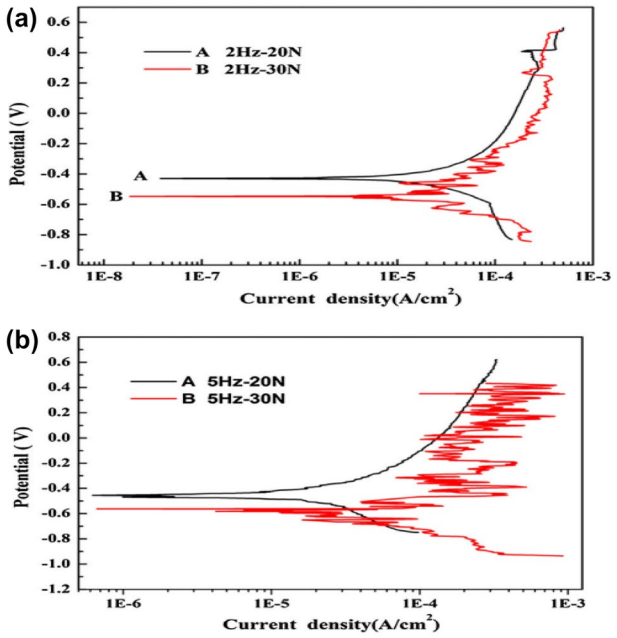

Fig. 6 The potentiodynamic polarization curves (Tafel curves) of Ti25Nb3Mo3Zr2Sn during tribocorrosion tests performed at 20N and 30N in phosphate-buffered solution for different sliding frequencies **a** 2 Hz and **b** 3 Hz [61]

$$I_t = I_0 \sin(wt + \phi) \tag{2}$$

It must be noted that small values of E_t are often applied to ensure the psuedo-linearity of the electrochemical system. If the system is not linear the response current will involve harmonics of the applied potential frequency (i.e. the frequency of the response current is a multiple of the frequency of the applied potential) [63]. The impedance of the whole system can be computed as follows:

$$Z = \frac{U}{I} = Z_0 \exp(i\phi) = Z_0(\cos(\phi) + i\sin(\phi)) \tag{3}$$

where Z is the impedance, Z_0 is the impedance magnitude and ϕ is the phase shift between E and I. The negative imaginary part of Z ($-Z_{\text{im}}$) is plotted as a function of the real part of Z (Z_{real}) at different excitation signals U frequencies to obtain what is called Nyquist plot that is shown in Fig. 8. Each point in the Nyquist plot corresponds to an impedance value at a certain frequency, but it is not possible to figure out the frequency utilized to record this point [63]. The frequency varies from small numbers close to zero to very high values. Each point on the Nyquist plot can be defined by a vector of amplitude $|Z| = ({Z_{\text{real}}}^2 + Z_{\text{im}}^2)$ and phase shift $\phi = arctan(\frac{Z_{\text{im}}}{Z_{\text{real}}})$. Therefore, the Nyquist plot can be represented in an alternative manner using Bode and phase shift plots that show the variation of |Z| and ϕ as function of the frequency, respectively (Fig. 9) [65].

During triboelectrochemical wear, various electrochemical processes take place and they can be simulated with an equivalent circuit that can include resistors, capacitors or inductors. The proper equivalent circuit elements are chosen and connected based on the Nyquist plot shape (Fig. 10). The latter is depicted by the working electrode material composition and the electrochemical reactions induced in the vicinity of the working electrode surface or in the solution. Furthermore, the specified electric elements must have a physical interpretation that corresponds to the physical and chemical processes taking place. The EIS measurements can be performed at different stages of the tribocorrosion test (Fig. 7) to deeply understand the electrochemical and physical processes taking place during the depassivation and the repassivation of the metallic material.

3.2 Quantitative Analysis of the Tribocorrosion Mechanism According to ASTMG119-09 and UNE112086 Standards

To have an insight on the tribocorrosion extent, the wear rate can be quantified [28]. To interpret the synergy between mechanical wear and corrosion, it is indispensable to compute the weight loss attributed to mechanical wear, corrosion and to the synergy between them. To properly achieve this, appropriate standards must be followed to accurately compute the different wear losses. The only two standards present in the literature and that are followed to quantitatively asses the tribocorrosion wear are the ASTM G119 standard and the standard proposed by Diomidis et al [66] and named as "UNE112086 standard" in [67].

3.2.1 The ASTM G119-09 Standards

3.2.1.1 Wear Rates Calculations in ASTMG119-09 The ASTM G119 standard presented in [68] may be followed to have a quantitative insight into the tribocorrosion wear mechanism. According to ASTM G119, the tribocorrosion wear rate is formulated as shown below [68, 69]:

$$K_{mc} = K_m + K_c = K_{mo} + K_{co} + \Delta K_m + \Delta K_c = K_{mo} + K_{co} + S \tag{4}$$

$$K_m = K_{mo} + \Delta K_m \tag{5}$$

$$K_c = K_{co} + \Delta K_c \tag{6}$$

where K_{mc} is the total tribocorrosion wear rate at OCP, K_m is the total mechanical wear rate and K_c is the total corrosion rate loss .K_{mo} is the pure mechanical wear rate in the absence of corrosion. K_{co} is the material loss rate attributed to pure corrosion. ΔK_m is the change in the mechanical wear

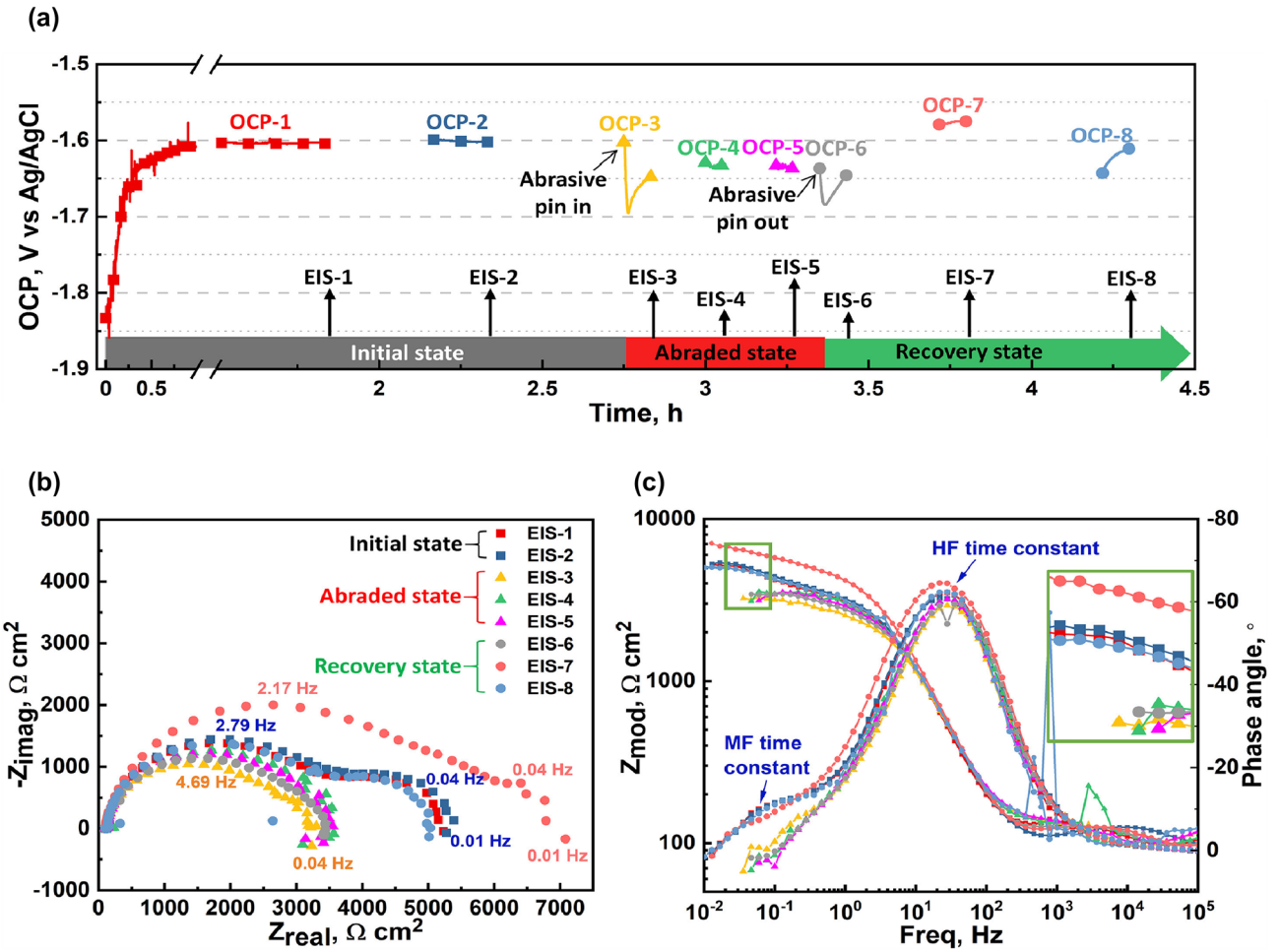

Fig. 7 EIS measurements performed at different stages of the tribocorrosion test on pure Mg. **a** OCP variation, **b** Nyquist plots and **c** Bode and phase plots [62]

rate due to corrosion and ΔK_c is the change in the corrosion rate due to mechanical wear where the sum of ΔK_m and ΔK_c represents the synergetic component (S). Physically speaking, ΔK_c is the wear rate attributed to the depassivation of the material via mechanical wear (wear accelerated corrosion). ΔK_m is the wear rate ascribed to the reaction of the wear particulates resulting from mechanical wear with the electrolyte to yield hard oxides that play the role of abrasive third bodies in the tribological system (corrosion accelerated wear) (Fig. 11).

K_{mc} is calculated as the material wear rate measured after the performance of a wear test in a certain electrolyte. The K_{mc} is calculated as follows:

$$k_{mc} = \frac{\text{Volume loss during tribocorrosion test}}{A_s \times t_{mc}} = \frac{m_{mci} - m_{mcf}}{\rho_{sp} \times A_s \times t_{mc}} \quad (7)$$

where m_{mci} and m_{mcf} are the masses in (g) of the working electrode (i.e.sample) before and after the tribocorrosion test, respectively. ρ_{sp} is the specimen density, A_s is the area of the specimen on which tribocorrosion wear test is done in (mm^2) and t_{mc} is the tribocorrosion wear test duration in years (yr) [68]. The k_{mo} is computed after performing a wear test on a cathodically polarized (1V cathodic with respect to the OCP) sample to avoid the corrosion of the working

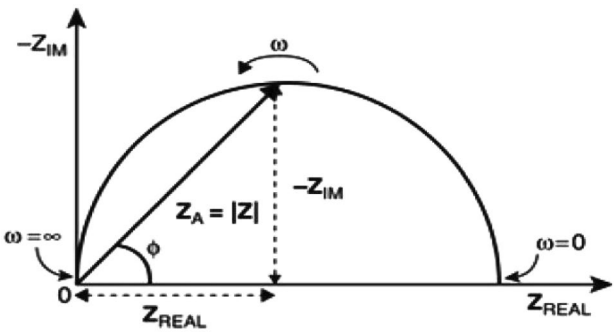

Fig. 8 Representation of the Nyquist diagram [64]

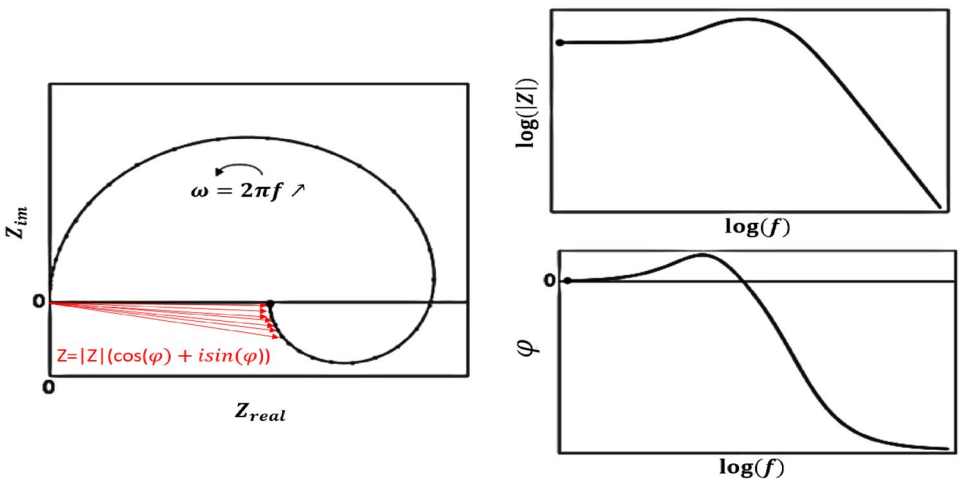

Fig. 9 Representation of the transformation from Nyquist representation to Bode and phase diagrams [65]

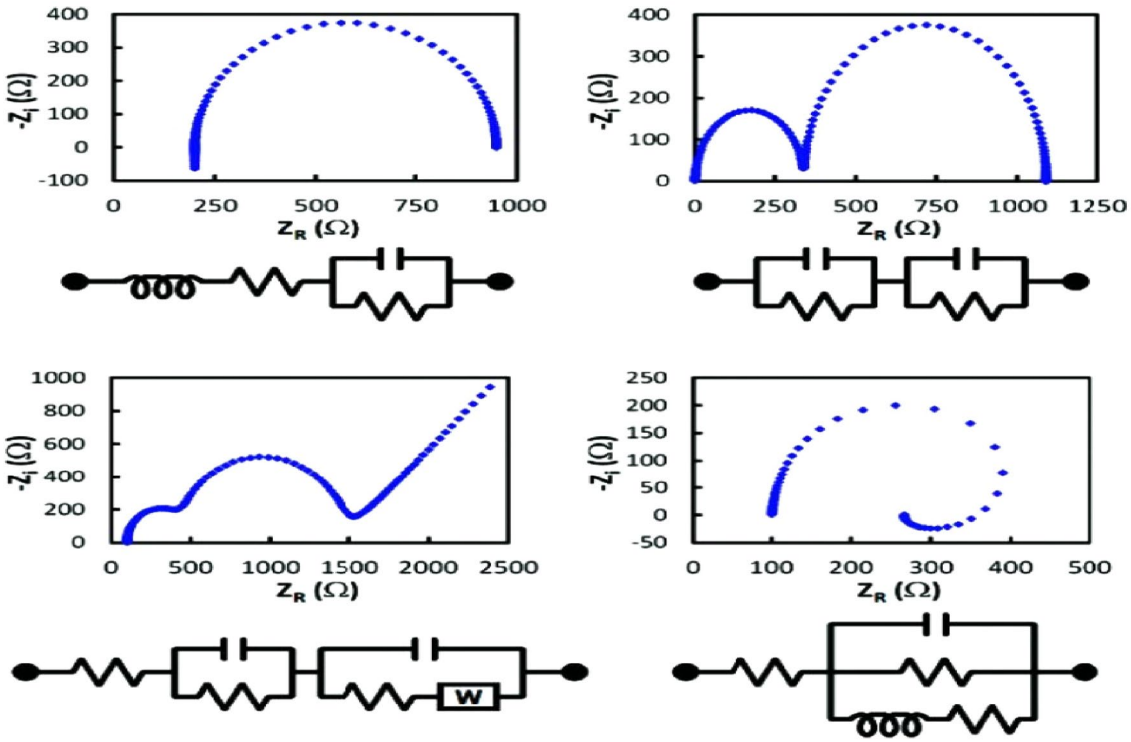

Fig. 10 Examples of various Nyquist plots and their corresponding equivalent circuits [64]

electrode. The k_{mo} can be calculated using the following formula:

$$k_{mo} = \frac{\text{Volume loss during tribocorrosion test on cathodically polarized working electrode}}{A_s \times t_{mo}} = \frac{m_{moi} - m_{mof}}{\rho_{sp} \times A_s \times t_{mo}} \quad (8)$$

where m_{moi} and m_{mof} are mass of the sample before and after conducting a tribocorrosion on the working electrode that is cathodically polarized, respectively. t_{mo} is the duration of the tribocorrosion test in which the sample is cathodically polarized [68]. The K_{co} and K_c can be calculated using the following form of Faraday's law:

$$K_{co} = C \times \frac{i_{co}}{A_s} \times E_w \quad (9)$$

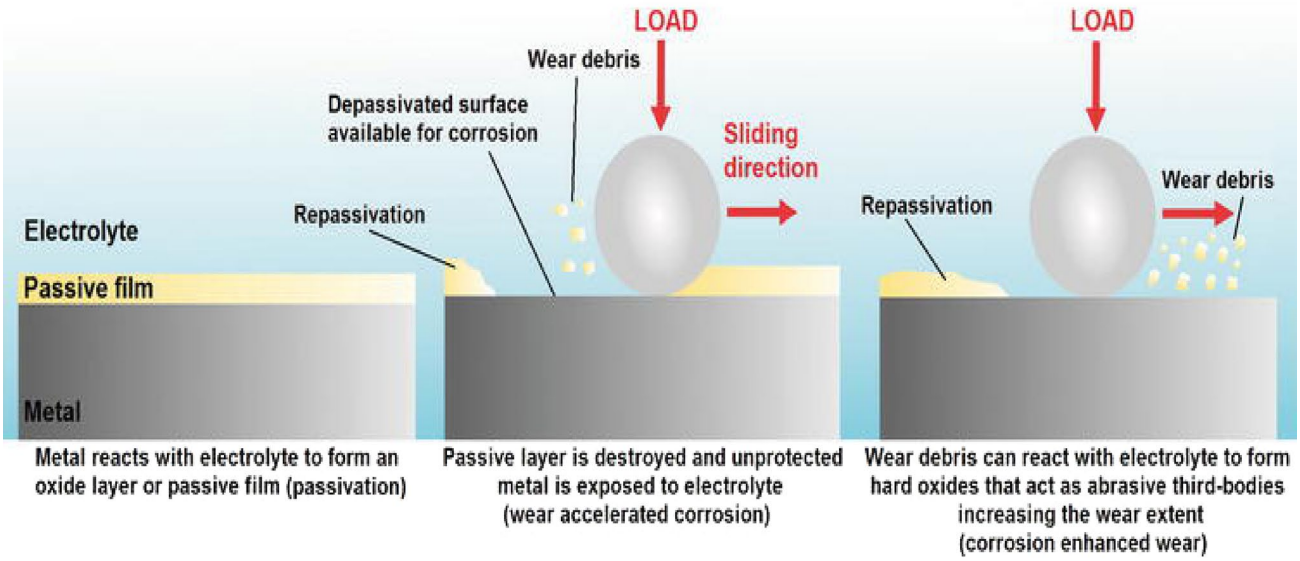

Fig. 11 The wear accelerated corrosion and the corrosion accelerated wear mechanisms. A schematic view of synergy between the mechanical wear and corrosion in the course of the tribocorrosion wear mechanism [72]

$$K_c = C \times \frac{i_c}{A_s} \times E_w \tag{10}$$

where i_{co} and i_c are the currents measured during a static corrosion test and tribocorrosion test, respectively. i_{co} and i_c are obtained from the Tafel curves recorded via potentiodynamic polarization. The corrosion current represents the intersection point between the asymptotes of the anodic and the cathodic part of the Tafel curve. C is a constant equals to $3.27 \times 10^{-3} \frac{mm \times g}{\mu A \times cm \times yr}$ that incorporates the Faraday constant and the conversion factors applied to express the corrosion rate in $\frac{mm^3}{mm^2 yr}$ [68]. E_w is the material equivalent weight which is defined as the mass of species that will react with one faraday of charge [70]. For pure metals, the $E_w = \frac{A_w}{n}$ where A_w is the atomic weight of the metal atom (e.g. Fe) and n is the number of electrons results from the dissolution reaction of the metal atom (e.g. n equals 2 for Fe dissolution). For an alloy that is subjected to uniform corrosion the E_w is computed as the molar weighted average of the equivalent weights of alloy components as shown below [71]:

$$E_{w_{alloy}} = \Sigma \frac{f_x \times n_x}{A_{w_x}} \tag{11}$$

where f_x and A_{w_x} are the mass fraction and the atomic weight of element x present in the alloy. Moreover, n_x is the number of electrons resulting from the dissolution of element x . After the computation of K_{mc}, K_{mo}, K_{co} and K_c, ΔK_c is calculated using Eq. 6. Moreover, ΔK_m and S can be computed using Eq. 6. It is important to note that in certain scenarios ΔK_m may be negative and this could be ascribed to the formation of a passive film that posses better wear resistance than the material [68] (e.g. TiO_2 has better wear properties than cp-Ti).

When all the wear rates are computed various dimensionless factors such as the total synergism factor (TSF), the corrosion augmentation factor (CAF), and wear augmentation factor (WAF) can be calculated as follows: [68, 73]:

$$TSF = \frac{K_{mc}}{K_{mc} - (\Delta K_m + \Delta K_m)} \tag{12}$$

$$CAF = \frac{K_{co} + \Delta K_c}{K_{co}} \tag{13}$$

$$WAF = \frac{K_{mo} + \Delta K_m}{K_{mo}} \tag{14}$$

These dimensionless factors depict the extent of the synergy between wear and corrosion [68].

3.2.1.2 Wear-Cororison Maps in ASTMG119-09 To understand the impact of certain material characteristics (e.g. average grain size, superficial residual stress and surface roughness) or experimental conditions (e.g. pH, reciprocation frequency and normal force) on the tribocorrosion behavior of the metallic part, it is indispensable to construct the wear corrosion maps. These maps are plotted by performing the wear rate calculations illustrated in the previous section for at least six tests that have different levels of the first investigated parameter. After that, for each one of the

six tests, another six test have different values of the second investigated parameter and a similar value of the first parameters are done and the wear rate computations are achieved for them. Then the K_{mc} is plotted as function of the two investigated factors and certain limits are defined for K_{mc} to classify the tribocorrosion extent that is high, medium or low. Furthermore the $\frac{\Delta K_c}{\Delta K_m}$ can be also plotted as a function of the studied paramters to understand how much the corrosion is impacting the wear and vice versa. If $\frac{\Delta K_c}{\Delta K_m} < 0.1$ then the wear augmentation by corrosion prevails (i.e. synergetic effect). however, if the $\frac{\Delta K_c}{\Delta K_m} \geq 1$ the corrosion augmentation by wear (i.e. additive effect) dominates. Nevertheless, if $0.1 \leq \frac{\Delta K_c}{\Delta K_m} < 1$ the synergetic and the additive effects have a similar extent [68].

The ASTM G119-09 standard was the principally deployed standard in the tribocorrosion studies. Nevertheless, according to some researchers, this standard may have some limitations. The ASTM G119-09 standard does not consider the galvanic coupling attributed to the discrepancy in the OCP of the worn and the unworn regions. Moreover, the deployed cathodic polarization during the investigation of the pure mechanical wear imposes the risk of hydrogen embrittlement which is pronounced in passivating materials more than in non-passivating ones. Furthermore, this cathodic polarization ignores the corrosion products that affect the wear mechanism at the OCP. Therefore, the ASTM G119-09 standard can be only employed in the tribocorrosion studies of non-passivating materials because it does not take into account the repassivation rate. An alternative protocol named as UNE112086 as stated in [74] was proposed by Diomidis et al. to assess the tribocorrosion behavior of the passivating materials [66].

3.2.2 The UNE112086 Protocol

In the UNE112086, the tribocorrosion tests are either implemented with continuous or intermittent sliding. The areas shown in Fig. 12b and c can be defined in the tribocorrosion tests with continuous and intermittent sliding, respectively. A_0 and A_{tr} are the area of the sample subjected to the tribocorrosion test and the wear track area, respectively. The active area (A_{act}) refers to the regions in which the passivated film is removed. The repassivated area corresponds to the regions where a worn material passivates and to the passive material that sustained the tribological actions. It is also important to define the following parameters for the tribocorrosion tests and they are the reactivity time (t_{reac}), the off time (t_{off}), latency time (t_{lat}), the rotation period (T_r) and the number of cycles (N). The t_{reac} is the time for the passive film to form. The t_{off} is the time for which the test stop after each cycle (N). The t_{lat} is the time between two consecutive contact actions at a certain point. The UNE protocol is divided into three main stages. First, The OCP is recorded, then the corrosion of the material covered by the passive film is analyzed. After that, The corrosion and the mechanical wear of the active material and the passive/repassivated material in the wear track are investigated, consecutively. Finally, the K_c and the K_m ratios are computed to assess the tribocorrrosion and the impact of the passivation on the mechanical wear. The stages are meticulously discussed in the upcoming paragraph.

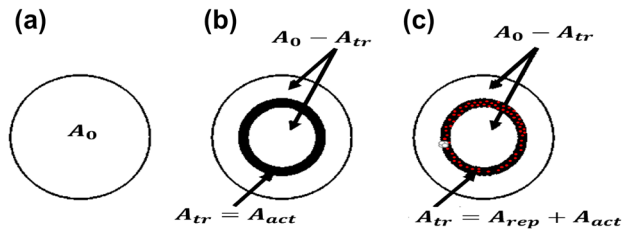

Fig. 12 **a** The area of the sample in which the tribocorrosion test is conducted. The worn area in tribocrrosion tests with **b** continuous sliding and **c** discontinuous sliding. The active, passivated and repassivated material are shown in black, white and red, respectively [66] (Color figure online)

The polished passivating material sample is submerged in the electrolyte and the OCP is recorded until a dynamic equilibrium is attained. The OCP is considered stable when the change of the OCP is below 1mV/min. The time until which the latter is satisfied is considered as the t_{reac} time. Stable OCP indicates that passivation takes place. After reaching a stable OCP, an EIS measurement is carried out to calculate the polarization resistance R_0 (the diameter of the typically obtained semi-circle in the Nyquist plot) which enables the computation of the corrosion density attributed to the corrosion of the material covered by the passive film (i_{pass}) as shown below:

$$i_{\mathrm{pass}} = \frac{B}{r_{\mathrm{pass}}} \tag{15}$$

$$r_{\mathrm{pass}} = R_0 A_0 \tag{16}$$

where B is a constant that is usually in the range of 13 to 35 mV for metals, r_{pass} is the specific polarization resistance and A_0 is the area subjected to corrosion. To analyze the corrosion and the mechanical wear of the active material, OCP is recorded until it is stable, then at this moment, a continuous sliding test is commenced so that the material in the wear track is mainly active. During the sliding, an EIS measurement is done to compute the polarization resistance of the specimen surface (R_1). The latter is an equivalent of the active area resistance R_{1act} and the unworn area $A_0 - A_{\mathrm{tr}}$ and the A_{rep} polarization resistance (R_{1pass}) as shown below:

$$\frac{1}{R_1} = \frac{1}{R_{1act}} + \frac{1}{R_{1pass}} \tag{17}$$

$$R_{1act} = \frac{r_{\text{act}}}{A_{\text{act}}} \tag{18}$$

$$R_{1pass} = \frac{r_{\text{pass}}}{A_0 - A_{\text{act}}} \tag{19}$$

$$r_{\text{act}} = \frac{A_{\text{tr}} R_1 r_{\text{pass}}}{r_{\text{pass}} - R_1 (A_0 - A_{\text{act}})} \tag{20}$$

where r_{act} and r_{pass} are the specific polarization resistance of the active and passivated area, respectively. It must be noted that in continuous sliding, the $A_{\text{tr}} \cong A_{\text{act}}$. Then, the corrosion density of the active material (i_{act}) is computed as follows [66]:

$$i_{\text{act}} = \frac{B}{r_{\text{act}}} \tag{21}$$

After calculating the i_{act}, the material loss ascribed to the corrosion of the active material is computed using Faraday's law as follows:

$$W^c_{\text{act}} = \frac{i_{\text{act}} A_{\text{act}} M N t_{\text{lat}}}{nF\rho} \tag{22}$$

where M and n are the molar weighted average of the molar mass of the alloy and of the number of electrons involved in the alloy dissociation, respectively. F is Faraday's constant 96500C, and ρ is the alloy density. After computing W^c_{act}, the volume of the wear track can be estimated using profilometry W_{tr}, then, W^m_{act} is calculated as follows:

$$W^m_{\text{act}} = W_{\text{tr}} - W^c_{\text{act}} \tag{23}$$

After investigating the active material, the corrosion and the mechanical wear of the passive/repassivated material are studied. This is done by conducting a discontinuous sliding test for $t_{\text{lat}} = 0.01 t_{reac}$ and $t_{\text{lat}} = 0.1 t_{reac}$ where $A_{\text{repass}} = 0.1 A_{\text{tr}}$ and $A_{\text{repass}} = 0.01 A_{\text{tr}}$, respectively. It is assumed that $\frac{A_{\text{repass}}}{A_{\text{tr}}} = \frac{t_{\text{lat}}}{t_{reac}}$. The wear volume attributed to the corrosion of the passive/repassivated material (W^c_{repass}), assuming that it exhibits a similar corrosion behavior to A_0 is computed as shown below:

$$W^c_{\text{repass}} = i_{\text{pass}} A_{\text{repass}} \frac{M}{nF\rho} N t_{\text{lat}} \tag{24}$$

After that, the mechanical wear of the passive layer (W^m_{repass}) is calculated as follows:

$$W^m_{\text{repass}} = W_{\text{tr}} - (W^c_{\text{repass}} + W^c_{\text{act}} + W^m_{\text{act}}) \tag{25}$$

After computing the various components of the total material loss, the specific material losses (w^j_i) can be calculated, where i can be "act" or "repass" and j can be "m" or "c". It must be noted that w^j_i is computed by dividing the material wear loss by N and the corresponding wear loss component area as shown below:

$$w^j_i = \frac{W^j_i}{N \times A^j_i} \tag{26}$$

To assess the tribocorrosion extent of the passivating materials and the effect of the passivating film on the mechanical wear, the K_c and K_m ratios are calculated, respectively, as follows:

$$K_c = \frac{W^c_{\text{act}} + W^c_{\text{repass}}}{W^m_{\text{act}} + W^m_{\text{repass}}} \tag{27}$$

$$K_m = \frac{w^m_{\text{act}}}{w^m_{\text{repass}}} \tag{28}$$

If $K_c > 1$ the material loss is mainly due to corrosion. If $K_c < 1$ the material loss is principally ascribed to mechanical wear. Moreover, if $K_c << 1$ the acceleration of corrosion due to the removal of the passive film is somehow very small with respect to the total wear loss. If $K_m > 1$ the passive film is somehow ameliorating the material wear resistance and the tribocorrosion extent is higher at low latency time. If $K_m < 1$ the passivation of the material deteriorates the wear resistance and augments the material loss. The tribocorrosion extent is higher at high latency time. Further explanations are presented in [66].

4 Tribocorrosion Performance of AM-ed Metallic Biomaterials in Hip Implant Application

In the literature, there are various studies that discuss the tribocorrosion of metallic biomaterials processed via conventional methods as in [59, 75–103]. Nevertheless, there are few studies that investigate the tribocorrosion of AM-ed biomaterials used in prosthetic hip implants such as Ti6Al4V [39, 104–106], Ti6Al4V-Si-Hydroxyapatite [107], Zr-based bulk metallic glass [11], 316L stainless steel [28], Ti-15Mo [108] and CoCrMo [109]. It was observed by Toptan et al. that the tribocorrosion performance of the SLM-ed Ti6Al4V parts is somehow similar to the one of the parts processed via hot pressing [104]. Nevertheless, the Ti6Al4V SLM-ed parts show a less stable oxide layer in the electrochemical experiments and this is attributed to the high content of the $\alpha'_{Ti6Al4V}$ Ti6Al4V martensite phase [104]. Moreover, a somehow smaller drop of the OCP is noticed for the SLM-ed Ti6Al4V alloy

compared to commercial forged Ti6Al4V, during the tribocorrosion test [106]. Due to the heterogeneous microstructure produced by SLM it is important to investigate the tribocorrosion resistance anisotropy. The latter was studied for Ti-15Mo SLM-ed alloy in a Hank's solution at 37 ± 0.5 °C. The tribocorrosion studies were done at planes oriented with 0, 45° and 90° as shown in Fig. 13a and c [108]. It was found that the tribocorrosion resistance in the 0° plane is higher than that in the 45° plane. Moreover, the tribocorrosion resistance in the 45° is higher than that in the 90° plane. This discrepancy in the tribocorrosion performance is ascribed to the presence of small amount of ω phase that possesses high hardness and that is present in the 0° but not in the 45° and 90° planes. Moreover, the relatively small grain size (Fig. 13a) and the high grain boundary density in the 0° plane (Fig. 13a) augment the superficial activity. Therefore, this may accelerate the repassivation of the material. It must be also mentioned that Dai et al. discovered that the corrosion resistance of the SLM-ed Ti6Al4V parts is anisotropic [110]. Chiu et al. detected Ti_3O and Ti_6O oxide in the small grain size $\alpha'_{Ti6Al4V}$ matrix of the SLM-ed Ti6Al4V. These microstructural features fortify the μ-hardness and consequently improve the wear resistance. Furthermore, it was found that the degradation mode of the SLM-ed Ti6Al4V parts is mainly adhesive wear, unlike the traditionally manufactured grade 5 Ti alloy which exhibits a third-body abrasive wear mode in SBF [105]. Stendal et al. showed that the 316L stainless steel SLM-ed parts have a lower ability than the wrought samples to accomplish an equilibrium between the mechanical wear and the compensation via the repassivation mechanism. Moreover, the increase in the corrosion rate during the wear test is higher for the SLM-ed part. Furthermore, it was found that the wear volume of the SLM-ed sample is lower than that of the wrought sample [28].

A study conducted by Buciumeanu et al. revealed that the tribocorrosion properties of the Ti6Al4V parts manufactured via the laser engineering net shaping (LENS) process are better than those of the casted or hot pressed parts [39]. Avila et al. also investigated the effect of the addition of Si and hydroxyapetite during the LENS

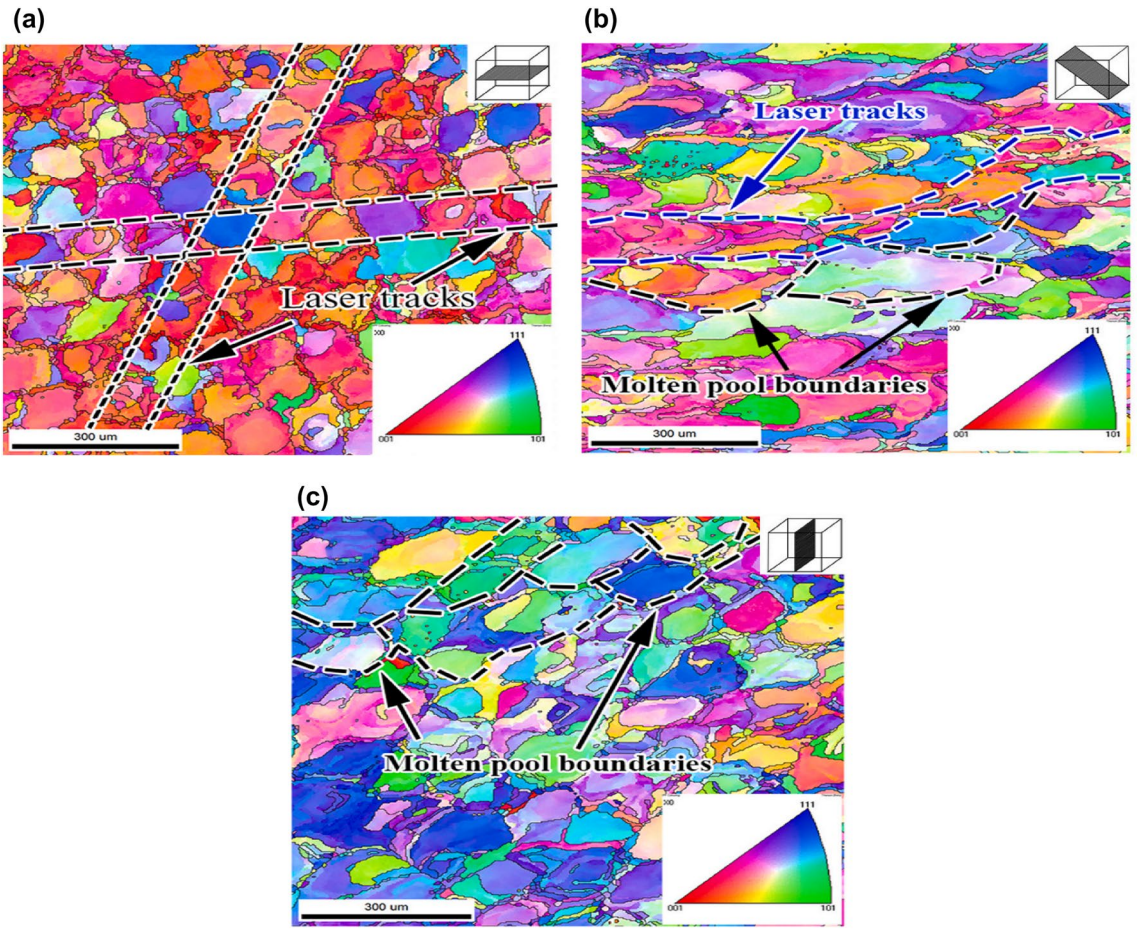

Fig. 13 EBSD maps of the microstructure of SLM-ed Ti–15Mo at **a** 0° **b** 45° and **c** 90° [108]

processing of Ti6Al4V on the tribocorrosion performance of the Ti alloy [107]. Liu et al. utilized an atomic force microscopy (AFM) tribocorrosion technique to compare the tribocorrosion of selective laser melted (SLM-ed) CoCrMoW and low carbon (LC) CoCrMo in phosphate-buffered saline (PBS) near the nanoscale. They found that the SLM-ed CoCrMoW exhibits higher levels of tribocorrosion than the LC CoCrMo. The cellular substructures in the SLM-ed CoCrMoW play a significant role in the tribocorrosion behavior. In the LC CoCrMo, the tribocorrosion wear depth mainly depends on the wear track size with respect to the grain size. Additionally, it was witnessed that the tribocorrosion was dependent on the applied contact pressure. When the latter is close to the hardness, no tribocorrosion was observed [111]. In some cases, the as-built (AB) AM-ed part is not competent enough to serve in the body's severe environment. Therefore, a post-treatment is required to boost the tribocorrosion performance of the AM-ed part. Potential post-treatments that may be applied to the AM-ed parts are presented in the next section.

5 Potential Post Treatments Applied to Enhance the Tribocorrosion Performance of AM-ed Metallic Biomaterials in a Hip Implant Application

In the literature, based on the author's knowledge, there are very few studies that investigate the effect of post-treatments on the tribocorosion of AM-ed metallic biomaterials for a hip implant application. Therefore, the post-treatments applied to enhance the tribocorrosion resistance of conventionally manufactured metallic biomaterials in a hip implant application are also discussed as potential post-treatments for AM-ed metallic biomaterials. Various post-treatments were investigated in the literature to augment the tribocorrosion performance, such as coatings. The coatings deposited are either diamond-like, carbon-based, metallic-based or ceramic-based coatings. Biofunctionalization treatments are also done on Ti based materials to enhance the tribocorrosion behavior and biocompatibility of the Ti-based metallic biomaterials. Moreover, nitriding, carburization, thermal oxidation and laser and mechanical post-treatments are done to enhance the tribocorrosion behavior of metallic biomaterials. The studies that investigate the effect of various post-treatments on the tribocorrosion resistance of metallic biomaterials in a hip implant application are presented in Table 1 and elaborated in the following sections.

5.1 Coatings to Enhance the Tribocorrosion Performance of Biomedical Parts

5.1.1 Diamond Like and Carbon Based Coatings

To ameliorate the tribocorrosion resistance of the metallic biomaterials, distinct protective layers can be deposited. These coating layers act as barriers that obstruct the infusion of the corrosion electrolyte and possess relatively high wear resistance. Grabarczyk et al. investigated various post-treatments (i.e. diamond-like coating (DLC), oxidation and carburization) of the Ti6Al4V. They discovered that the superficial oxidation followed by the DLC coating functionalization significantly enhances the tribocorrosion performance of Ti6Al4V alloy while preserving good mechanical properties [112]. Moreover, the DLC coatings restrict the release of implant metal ions into the body [144]. It must be noted that the DLC coating is biocompatible in vivo and in-vitro environments [145]. The DLC films provide a convenient hosting environment for the development of cells (i.e. fibroblasts, osteoblasts and macrophages) without any sign of cytotoxicity or inflammation. They also inhibit thrombogenicity and enhance blood compatibility [144]. The DLC coatings are also employed to functionalize 316L stainless steel parts, however, a bonding interlayer (i.e. plasma nitrided layer (PNL) or amorphous hydrogenated silicon nitride ($a-SiN_x:H$) layer) is required to improve the adhesion between the coating and the substrate. It was found that the PNL enhances the tribological behavior but not the tribocorrosion performance of the DLC layer. This is attributed to the infiltration of the electrolyte (e.g. Ringer's solution) via the voids to corrode the interface between the substrate and the bonding layer. Consequently, the tribo-electrochemical properties are deteriorated . Nonetheless, the $a-SiN_x:H$ enhances the tribocorrosion performance by somehow obstructing the flow of the electrolyte to the interface. Therefore, the probability of interfacial debilitation decreases [113]. It must be mentioned that there are various contradictory results in the literature regarding the effect of the DLC coating on the wear resistance of biomedical implants. This is attributed to the distinct experimental setups and conditions deployed in the analysis of the tribocorrosion resistance of the biomaterials [144]. carbide derived carbon (CDC) coatings are also used to functionalize the Ti6Al4V alloy against tribocorrosion in biological environment (i.e. bovine calf serum). It was found that the CDC functionalized Ti6Al4V alloy exhibits a lower COF, OCP drop and wear volume compared to the bare Ti6Al4V alloy. Moreover, the biocompatibility of the CDC coatings was also confirmed by Cheng et al. via cell proliferation experiments [115].

Table 1 Research works that investigate the impact of post-treatments on the tribocorrosion behavior of metallic biomaterials utilized in a hip implant application

Counter body	Motion type and tribometer	Solution	Normal force	Frequency or speed	Substrate	Post treatments
Alumina ball	Linear reciprocation (ball on disc)	Phosphate buffered saline (PBS) pH=7.4 at 37 °C	2N	1 Hz	Ti6Al4V	Thermochemical treatments (i.e. oxidation and carburization), Diamond like coating (DLC) deposition [112] ⋄
Alumina ball	Linear reciprocation (ball on flat)	Ringer's solution $pH \approx 6.6$	9N (1.18 GPa Hertzian pressure)	1 Hz	316L stainless steel	DLC deposition, amorphous hydrogenated silicon nitride layer deposition and plasma nitiriding [113]⋄
Alumina ball	Rotation (pin on ball) [114, 115]	Bovine calf serum (BCS) solution at pH=7.6	16N (50–250 MPa contact pressure)	1 Hz	Ti6Al4V	Carburization and chlorination [114]⋄
Alumina ball	Reciprocation (ball on disc)	Hank's solution 25 ± 3 °C $pH = 7.5 \pm 0.5$	1N (maximum contact pressure ≈ 3 GPa)	1 cm/s	Ti6Al4V	Multilayer Ta/ZrN thin coatings produced via reactive radio frequency magnetron sputtering [116]△
Si_3N_4 ball 6 mm diameter	linear reciprocation (ball on disc) microtribometer	3.5 wt% NaCl solution	1N	1 Hz	304 stainless steel	TiAlCN/ TiAlN/ TiAl multilayer composite coatings via filter cathodic vacuum arc technique [117]△
Alumina ball 10 mm diameter	Reciprocation CETRUMT2 Tribometer	simulated body fluid(SBF)+ bovine serum albumin (pH=7.4 at 36.5 ± 1.5 °C)	1N and 2N Hertzian maximum contact pressure (575 MPa and 724 MPa)	1 Hz	CoCrMo	Multilayer coating of alternating TiAlVCN and a-CN_x produced via magnetron sputtering [118]△
Alumina ball 10 mm diameter	Reciprocation (ball on plate)	9g/l NaCl solution	1N	1 Hz	Ti substrate	Nb and Mo diffusion treatments [119]△
Alumina ball 4 mm diameter	Rotation (ball on disc)	SBF at 37 ± 1 °C 50% relative humidity	5N Hertzian contact pressure 1 GPa	10 cm/s	Ti–13Nb–13Zr alloy	Filtered-arc- deposited Ta coating [120]△
Alumina ball	Rotation (pin on ball)	BCS	16N (50 MPa contact pressure)	1 Hz	Ti6Al4V alloy	Plasma sprayed ceramic coatings [121]♣
Si_3N_4 ball 6mm diameter	Linear reciprocation (ball on flat)	3.5 wt% NaCl solution pH=7.05 19 − 20 °C	20N (1.8 GPa Hertzian pressure)	300 slide per min	304 stainless steel	Ytrria- stabalized zirconia(YSZ) coating via atmospheric plasma spraying [122]♣
SiC ball 5 mm diameter	Linear reciprocation (ball on disc)	PBS pH= 7.4 ± 0.1	5N	1 Hz	Zr2.5Nb alloy	$ZrO_2 - Al_2O_3$ composite coatings via plasma electrolytic oxidation [123]♣
Sapphire ball 6 mm diameter	Rotation (pin on disc)	0.9% NaCl solution (pH = 7.4) 37 ± 0.5 °C	5N	15 cm/s	316L stainless steel	TiC, ZrC,TiNbC cathodic arc evaporation method [124]♣
SiC ball 7 mm diameter	–	0.9 wt% NaCl 37 ± 1 °C	5N	1 Hz	cp-Ti and Ti6Al4V alloy	Micro-arc oxidation [125]♠
Alumina ball 10 mm diameter	Reciprocation (ball on plate)	PBS 37 ± 2 °C	1N	1 Hz	Ti reinforced with Al_2O_3	Micro-arc oxidation [126]♠

Table 1 (continued)

Counter body	Motion type and tribometer	Solution	Normal force	Frequency or speed	Substrate	Post treatments
Alumina ball 10 mm diameter	Reciprocation (pin on disc)	8g/l NaCl solution	1.5N	2 Hz	Commercially pure (cp) Ti (grade 2)	Anodic treatment [127]♠
Alumina ball 6 mm diameter	Linear reciprocation	SBF 37 °C	2N	–	Ti6Al4V alloy	Micro-arc oxidation [128]♠
–	Reciprocation (ball on flat)	PBS	–	–	cp-Ti	Plasma electrolytic oxidation♠ and annealing at 600 °C for 1 hour [129]
Alumina ball 7 mm diameter	Linear reciprocation	Ringer's solution	5N	1 Hz	Ti6Al4V	Micro-arc oxidation [130]♠
Alumina sintered ring with 22.5 mm outer diameter and a width of 13.5 mm	Rotation (block on ring)	Hanks' physiological solution at 37 °C	2N	100 rev/min or 0.12 m/s	Ti6Al4V alloy	Anodic oxidation + hydroxyapatite (HA)/nano $-TiO_2$ coating [131]♠
Alumina ball 10 mm diameter	Linear reciprocation (pin on plate)	PBS 37 °C ± 2	0.5N	1 Hz	Ti–40Nb alloy	Two step anodic treatment♠ +heat treatment+ TiO_2 nanotubes♠ [132]
Alumina ball 10 mm diameter	Reciprocation	PBS 37 °C	1N	1 Hz	Ti25Nb5Fe alloy reinforced with 5% vol TiN particles	Micro-arc oxidation [133]♠
Alumina ball 10 mm diameter	Reciprocation (ball on plate)	PBS 37 °C	6N	1 Hz	Ti6Al4V alloy	Poly-ether-ether ketone via hot pressing [106]♠
Alumina ball 6 mm diameter	Reciprocation (ball on flat)	Kokubo's SBF 37 °C	5N	1 Hz	cp-Ti grade 2	Plasma nitriding⊗+ anodization [134]♠
Alumina ball 10 mm ball	Reciprocation	PBS 37 °C	0.5N	1 Hz	Ti–12Nb alloy	Radio Frequency (RF) sputtering technique in Nitrogen atmosphere [135]⊗
Alumina ball 7 mm diameter	Reciprocation (ball on flat)	Hank's solution 37 °C	2N	0.92 m/min	Medical pure Ti alloy (TA1)	Nitriding via high-frequency electromagnetic induction heating [136]⊗
Alumina ball 8 mm diameter	Rotation (pin on disc)	0.9% NaCl solution room temperature	20N (maximum Hertzian contact pressure (1291MPa) max shear stress (391MPa) at 42μm from the surface)	60 rev/min	cp-Ti grade 2	Thermal oxidation and pack carburisation with limited oxygen diffusion [137]⊙
Alumina ball 6 mm diameter	Linear reciprocation (ball on flat)	0.9 wt% NaCl solution room temperature	5N maximum hertzian pressure 0.64GPa	1 Hz	Ti6Al4V alloy	Thermal oxidation [138]⊙
Alumina ball	Rotation hip simulator tribometer	BCS 37 ± 1 °C	20N	1 Hz	Ti6Al4V alloy	Carburization [114]⊙

Table 1 (continued)

Counter body	Motion type and tribometer	Solution	Normal force	Frequency or speed	Substrate	Post treatments
Alumina ball	Rotation (pin on disc)	0.90 wt% NaCl solution room temperature pH 6.5	2N (Herztian pressure of 410 MPa)	75 rev/min	Ti6Al4V alloy	Laser remelting treatment [139]♭
Alumina ball	Reciprocation (pin on disc)	3.5% NaCl solution (pH 6.24) modified 3.5% NaCl solution (pH 4) 22 °C ± 2	5N	5 Hz	Ti6Al4V	Laser cladding of cp-Ti [140]♭
Alumina ball 6.35 mm diameter	Reciprocation (ball on disc)	3.5% NaCl solution 25 °C 15% relative humidity	20N	1 mm/s	AZ31B Magnesium alloy	Laser shock peening [141]♭
Bearing steel ball 6.35 mm diameter	Reciprocation (ball on disc)	3.5% NaCl solution	10N	2 Hz	Selective laser melted CoCrMo alloy	Ultrasonic nanocrystal surface modification [109]♮
Alumina ball 6 mm diameter	Reciprocation	3.5 wt% NaCl solution ~ 22 °C 50% relative humidity	3N	–	AISI 4140 low-alloy steel	Shot peening [142]♮
Alumina ball 8 mm diameter	Rotation (pin on disc)	0.9 wt% NaCl solution 22 °C	10N,20N and 40N maximum contact pressures (1270 MPa, 1600 MPa, 2015 MPa	60 rev/min	304 austenitic stainless steel	Surface mechanical attrition treatment [143]♮

⋄ Corresponds to the family of diamond and carbon like coatings,△ the family of metallic coatings, ♣ ceramic coatings, ♠ biofunctionalization post-treatments, ⊗ Nitriding processes,⊙ oxidation and carburization treatments, ♭ laser treatments and ♮ mechanical post treatments

5.1.2 Metallic Based Coatings

Biocompatible metallic materials can be also deposited to improve the tribocorrosion performance of biomedical parts. Metallic Ta and ZrN layers were deposited with various thickness configurations on Ti6Al4V substrate. During the tribocorrosion test of this coated substrate in Hank's solution, a slight increase in the OCP was detected. This suggests that such coatings have somehow a good tribocorrosion performance. It was also found that the composite layer with the highest hardness to elastic modulus ratio (H/E) exhibits the best tribocorrosion performance [116]. The H/E ratio is a plastic deformation index utilized to asses the tribological behavior of the coating material. If the H/E is high, the elastic strain to failure of the coating layer is high. The tribocorrosion performance of TiAlCN/TiAlN/TiAl multilayer coatings deposited on 304 stainless steel via filter cathodic vacuum arc technique with distinct carbon contents was tested. The multilayer with 12.4% carbon content showed the smallest OCP drop (0.003V) and the lowest COF (0.07) in 3.5% NaCl solution among the multilayers with 0, 8.6 and 22.1% carbon content. This is because the dense multilayer microstructure with 12.1% C content possesses the highest hardness and H/E ratio and exhibits stable passivation. It's high hardness is due to the balanced fraction of the amorphous C phase present in the vicinity of the grain boundaries. This amorphous phase obstructs the dislocation motion [117]. Alemon et al. investigated the effect of TiAlVCN/CN_x multilayer (Fig. 14) on the tribocorrosion of CoCrMo alloy in SBF containing bovine serum albumin. It was observed the CN_x amorphous upper layer helps in decreasing the COF. Moreover, it protects the material against localized corrosion (i.e pitting corrosion). Thus, the number of pits that can act as crack initiation sites during tribocorrosion is decreased. Furthermore, the TiAlVCN/CN_x coated substrate achieved a lower OCP drop than the bare one, during the tribocorrosion test. Moreover, it was seen that the TiAlVCN/CN_x multilayer coating decreases six to seven times the material wear rate and acts as a diffusion barrier for the metallic ions [118].

Ureña et al. investigated the effect of Nb and Mo diffusion treatments on the tribocorrosion performance of grade 4 commercially pure Ti (cp-Ti) as-pressed and sintered substrates that were obtained via powder metallurgy and diffusion treated with Mo or with Nb as illustrated in [119]. Hee et al. investigated the impact of the filtered-arc-deposited Ta coating on the tribocorrosion behavior of Ti13Nb13Zr alloy and they found that it is not convenient for implant applications [120].

5.1.3 Ceramic-Based Coatings

In the literature, ceramic-based films are proposed as candidates to improve the tribocorrosion of biomedical hip implants. Cheng et al. investigated the tribocorrosion resistance of Ti6Al4V that is plasma sprayed with hard ceramic coatings (i.e. conventional monolithic micron alumina (IDA), micron alumina- 40 wt% ytrria- stabalized zirconia (YSZ) composite coating (IDAZ) and bi-layer nanostructured alumina -13 wt% titania/ YSZ (IDZAT)) for hip implant application. It was observed that these ceramic coatings were somehow not influenced by the tribocorrosion mechanism due to their chemical inertness and high insulation. The main factor that impacts the competency of these coatings is the porosity content. The pores act as sites for the localized corrosion via the capillarity mechanism. During the latter, the electrolyte flows into the voids and results in the degradation of the substrate-coating interface. Consequently, the coating may blister and its adhesion to the substrate becomes vulnerable. It must be noted that the capillarity mechanism is dominant for a porosity content higher than 2%. Moreover, it was observed that during the tribocorrosion test, the IDZAT is the noblest coating among the others and it exhibits the lowest COF. It must be mentioned that there are various limitations for that study and they are presented in [121]. The tribocorrosion resistance of YSZ plasma sprayed 304 stainless steel in 3.5wt% NaCl solution

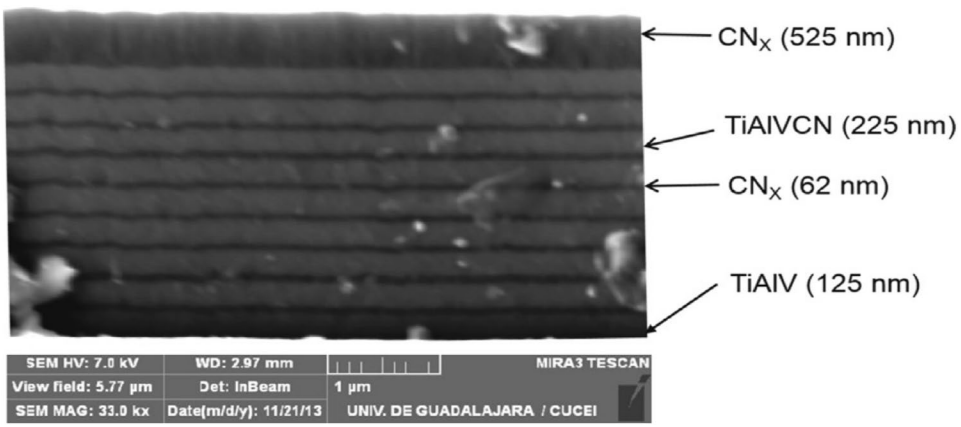

Fig. 14 TiAlVCN-CNx multilayer coatings [118]

was also investigated in [122]. Other ceramic-based coatings such as $ZrO_2Al_2O_3$ composite coatings were investigated in the literature. Sourani et al. studied the tribocorrosion resistance of $ZrO_2Al_2O_3$ coatings in phosphate-buffered saline (PBS). The coatings were created via plasma electrolytic oxidation (PEO) on the surface of Zr-2.5Nb substrates, using various bipolar waveforms with 10%, 20% and 40% cathodic duty cycles for 6min. They observed that the $ZrO_2Al_2O_3$ coating corresponding to the treatment done with 40% duty cycle exhibits no OCP drop. Additionally, it has a relatively low arithmetic mean height (R_a) 0.35 ± 0.06 and it showed the lowest wear volume $0.035mm^3$. The latter is attributed to the relatively high hardness of the coating ($1264 \pm 21HV_{1000}$) and to its compactness. It is important to note that adhesion and delamination were the dominant wear mechanisms in this study [123]. ZrC, TiNbC and TiC are used as coatings to functionalize 316L stainless steel parts that are used in load bearing applications. It was observed that the ZrC and the TiNbC show a better mechanical, corrosion and tribocorrosion performance than TiC coatings. Nevertheless, the TiNbC is the best candidate for biomedical applications due to the combination of low friction coefficient and good corrosion properties [124].

5.2 Biofunctionalization

Functionalizing the surface to protect it against tribocorrosion is not sufficient for biomedical parts that will be implemented in side a complex and sensitive biological environment. Therefore, the biofunctionalization of biomedical parts is crucial to ensure their biocompatibility and their proper biomedical functioning. Surface biofunctionalization of the biomedical implant is achieved to improve the interaction of the material with the osteoblasts that are responsible for bone formation [146]. Micro arc oxidation (MAO) is a method that is commonly deployed to integrate bioactive elements (e.g. P, Zn and Ca) present in an electrolyte into the created oxide layer that is not sufficiently bioactive [130, 147].

5.2.1 Biofunctionalization of cp-Ti and Ti6Al4V

The cp-Ti and the Ti6Al4V alloy are extensively used as materials in hip implant applications. Nevertheless, such materials may not be sufficiently bioactive to accomplish a proper osseointegration. Therefore, they are biofunctionalized. Fazel et al. studied the effect of the MAO treatment on the tribocorrosion of cp-Ti and Ti6Al4V. The latter were MAO-ed in 1.8M H_2SO_4-0.4M H_3PO_4 at room temperature and at 180V. This treatment leads to the formation of an oxide layer of volcanic morphology on the surface of the cp-Ti sample (Fig. 15a, c) and to the creation of an oxide film of cortex-like morphology with irregular vermiform slots on the Ti6Al4V sample (Fig. 15b, d). It was found that the MAO enhances the tribocorrosion behavior of the treated materials. It was also observed that abrasive degradation is

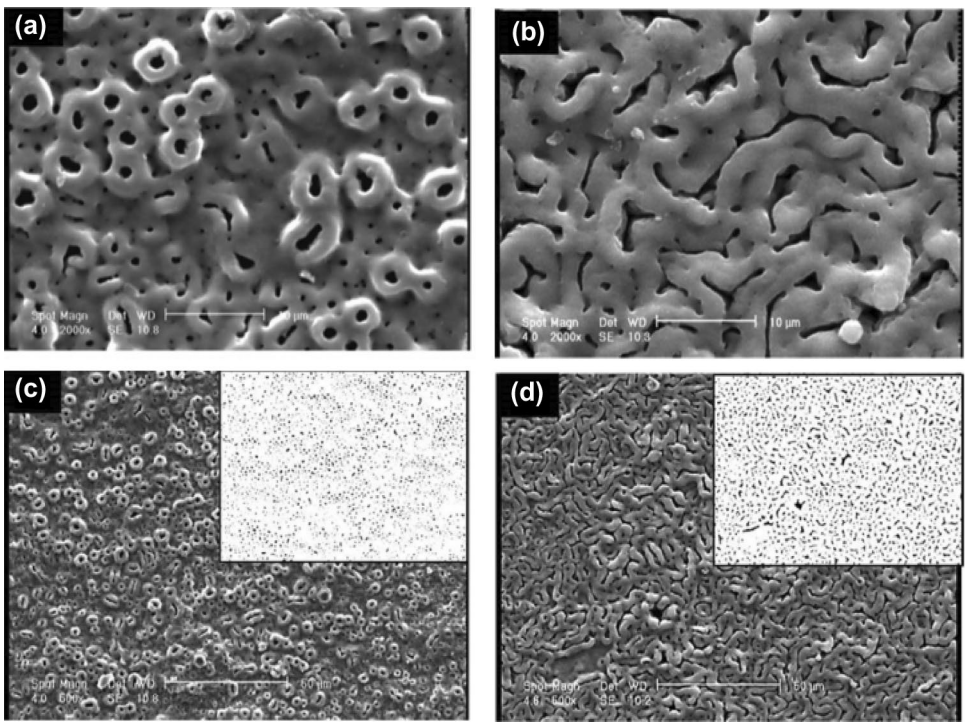

Fig. 15 The morphology of the oxide layer formed on the surface of **a** cp-Ti and **b** Ti6Al4V after MAO [125]

the main wear mode in the tribocorrosion of the MAO-ed Ti6Al4V in 0.9wt% NaCl solution at 37 ± 1 °C. Nevertheless, during the tribocorrosion testing of MAO-ed cp-Ti, fretting fatigue takes place and it yields the delamination of the oxide film [125]. Sousa et al. proposed a MAO treatment done at 300V for 1 min in a turbulent electrolyte that contains 0.35M of calcium acetate monohydrate and 0.02M of glycerophosphate disodium salt pentahydrate to post-treat Ti and $TiAl_2O_3$ composite samples processed via powder metallurgy at 1000 °C and at 1100 °C. It was found that such MAO treatment ameliorates the tribocorrosion performance of Ti and $TiAl_2O_3$ composite in PBS at 37 ± 2 °C. This is mainly ascribed to the formed hard rutile and anatase phases that improve the wear resistance. It must be remarked that for the Ti grade2 powder sintered at 1000 °C, the volcanic morphology is eliminated after the tribocorrosion test [126].

In the literature, there are many studies that focus on the effect of a certain biofunctionalization parameter on the tribocorrosion performance of cp-Ti and Ti6Al4V materials. Alves et al. studied the effect of the variation in the Ca/P ratio on the tribocorrosion behavior of the anodic treated cp-Ti in 8*g*/*l* NaCl solution. Varying the Ca/P ratio in the oxide (i.e. 1.57 ± 0.14 and 3.53 ± 0.14) film was accomplished by changing the concentration of calcium acetate in the electrolytic solution (i.e. 18.68 and 39.34) that was utilized to perform the anodic treatment. It was observed that changing the Ca/P ratio alters the morphology and the chemical structure of the surface. It was shown that the sample with higher Ca/P ratio exhibits a better tribocorrosion performance than the one with lower Ca/P ratio. This may be attributed to the fact that TiO_2 rutile and anatase phases were detected in the sample that was anodized in the solution with a higher Ca/P ratio. Nevertheless, in the sample corresponding to the lower Ca/P ratio, mainly anatase phase was indexed. The additional rutile phase present in the sample with a higher Ca/P ratio possesses a hardness (17GPa) that is somehow twice that of the anatase phase (8GPa). It must be noted that the augmentation in the hardness of the sample that have an oxide film with a higher Ca/P ratio is not associated with a drastic increase in brittleness [127]. Alves et al. discussed the biofunctionalization of cp-Ti grade 2 with Ca and P rich oxide layer via PEO. It was observed that the electrolyte composition used in the PEO impacts the tribocorrosion properties of the biofunctionalized material. The higher the resultant rutile to anatase fraction in the treated material, the better the tribocorrosion performance. The roughness, thickness, porosity content, crystallinity and the chemical composition of the rutile-anatase TiO_2 film created after PEO can be monitored either by tuning the PEO parameters or by applying a thermal treatment at a temperature higher than 400 °C [129, 148]. Laurindo et al. investigated the impact of the heat treatment at 600 °C for 1h and the effect of the PEO voltage (i.e. 300V and 400V) on the tribocorrosion performance of the oxide layer formed after the PEO treatment of cp-Ti for 1min in an electrolyte containing Ca and P. They found that the heat treatment augments the fraction of the rutile phase in the oxide film, especially in the sample PEO-ed at 300V. This phase composition modification may play a role in improving the mechanical performance of the inner oxide layer. Consequently, the tribocorrosion performance in PBS was enhanced [129]. It was also found that the addition of 10mL/L graphene oxide to the electrolyte of the MAO treatment achieves the best improvement to the tribocorrosion behavior of Ti6Al4V in 3.5% NaCl aqueous solution among the other dozes of graphene oxide (i.e. 0,5 and 15mL/L) [149].The effect of the temperature on the tribocorrosion performance of MAO treated Ti6Al4V alloy was investigated in [130]. It was observed that deploying the MAO treatment on Ti6Al4V at a low temperature (−3 °C) yields a compact oxide layer with quasi-filled voids. This film involves a relatively higher fraction of rutile TiO_2 phase that plays the role of a solid lubricant. Consequently, the tribocorrosion behavior of the material in Ringer's solution was improved [130].

Anodic oxidation treatments may be also applied on the Ti6Al4V alloy prior to further functionalization. Lee et al. investigated the effect of hydroxyapatite(HA)/nano-TiO_2 composite coating on the tribocorrosion of anodized Ti6Al4V. The anodic oxidation treatments done at 10V and at room temperature for various anodizing durations (i.e. 0,40,50,60,120 and 180 min) in 1M H_3PO_4 electrolyte were carried out to improve the adhesion of such a coating to the Ti6Al4V substrate. It was observed that the coating deposited on the substrate that was anodized for 180 min exhibits the best tribocorrosion performance in Hank's solution [131]. Bioabsorbable polymer coatings such as poly (D,L-lactic acid) can also be a convenient candidate for biomedical implants (hip or dental implant). It is worth noting that such coatings can boost the tribocorrosion performance of Ti6Al4V alloy in artificial saliva. It can also play the role of a solid lubricant that incorporate therapeutic materials on the surface of an endosseous implant. It must be remarked that such a coating layer will be continuously absorbed in the course of the osseointegration and it will release the therapeutic substances [150].

5.2.2 Biofunctionalization of Other Ti Alloys

The Ti6Al4V is widely used as a hip implant material, however, this alloy contains V which is a toxic element and Al whose presence may be accompanied by the Alzheimer disease. Therefore, β type Ti alloys such as Ti40Nb are being investigated as an alternative to Ti6Al4V. Nevertheless, this alloy exhibits poor tribological and tribocorrosion properties. Hence, TiO_2-based nanotubular (TNT) surfaces are created on such alloys to improve their tribocorrosion

properties. The TNT layer vulnerable point is that it exhibits a poor adhesion to the substrate. Çaha et al proposed a double step anodic treatment followed by a thermal treatment to resolve this issue. They discovered that the second anodic treatment done in fluoride free electrolyte yields an oxide film at the interface of the TNT layer with the substrate and gigantically ameliorates the TNT layer adhesion. They also observed that the heat treatment induces a crystalline transformation. The latter significantly enhances the tribocorrosion performance of the Ti40Nb alloy [132]. Çaha et al. investigated the biofunctionalization of TiN reinforced β Ti25Nb5Fe alloy via MAO. They found that the incorporation of TiN powder in β Ti25Nb5Fe alloy enhances the tribocorrosion performance which is further ameliorated by biofunctionalization via MAO treatment. The latter results in the formation of P and Ca rich thick rutile-anatase TiO_2 oxide layer on a consolidating hard $TiN_{0.3}$ phase. This layer ameliorates the tribocorrosion properties of the material in PBS at body temperature [133].

5.2.3 Biofunctionalization of AM-ed Metallic Biomaterials

Even though there are many studies that investigated the tribocorrosion of biofunctionalized metallic biomaterials, there are few papers that discuss the effect of biofunctionalization on the tribocorrosion of metallic AM-ed biomaterials used in hip implant application. Bartolomeu et al. investigated the tribocorrosion performance of SLM-ed perforated Ti6AL4V part that was impregnated with poly-ether-ether ketone (PEEK) via hot pressing. The PEEK has a high wear and corrosion resistance, however, it has a relatively low elastic modulus ($E = 3.6GPa$) compared to that of the cortical bone. Therefore, a Ti6Al4V-PEEK multimaterial structure is utilized. Bartolomeu et al. found that the PEEK that is located in the holes of the Ti6Al4V cellular structures plays an important role in enhancing the wear resistance. Moreover, they observed that the Ti6Al4V-PEEK cellular structures have a better tribocorrosion performance than that of the untreated SLM-ed Ti6Al4V cellular structures [106].

5.3 Nitriding, Carburization and Thermal Oxidation

5.3.1 Nitiriding

Nitriding may be deployed to ameliorate the tribocorrosion behavior of the biomaterials. The impact of the plasma nitriding and duplex treatment (i.e nitriding followed by anodic oxidation) on the tribocorrosion behavior of cp-Ti in SBF is discussed in [134]. it was found that the nitriding process results in the formation of TiN and T_2N phases that increase the superficial hardness and decrease the COF and the wear rate. The duplex treatment of the cp-Ti yields a porous TiO_2 layer that may enhance the osseointegration. This layer results in a good corrosion resistance. The duplex treated cp-Ti samples exhibits a better tribocorrosion performance than the plasma nitrided and the untreated specimens [134]. It was also observed that the radiofrequency-sputtered TiN coating does not improve the tribocorrosion resistance of the Ti12Nb alloy in PBS at the body temperature. Nonetheless, the deposition of ZnO layer on the Ti12Nb/TiN system enhances the tribocorrosion performance of the alloy [135]. Gaun et al. studied the effect of nitriding via a high frequency electromagnetic induction heating device on the tribocorrosion performance of medical pure Ti alloy in Hank's solution at 37 °C. TiN, Ti_2N and $TiN_{0.3}$ phases were detected in the nitrided sample. Moreover, the hardness of the nitrided material is six times higher than that of the bare one. It was also observed that nitriding reduces 20 times the mass loss during tribocorrosion and decreases 10 times the wear scar depth. Furthermore, the biocompatibility of the nitrided samples was assessed using L929 cells and it was proven that the nitriding film is not toxic [136].

5.3.2 Oxidation and Carburization Treatments

Oxidation and carburization of metallic biomedical alloys may lead to the precipitation of hardening phases that are nobler and that increase the material's superficial hardness. The effect of the thermal oxidation (TO) and pack carburization with limited oxygen diffusion (PCOD) treatments on the tribo-electrochemical behavior of cp-Ti in 0.9% NaCl solution was investigated in [137]. It was observed that the TO results in a rutile TiO_2 layer and the PCOD treatment creates a TiC network. It was found that the PCOD treated sample exhibits the best tribocorrosion behavior due to the adherent TiC network present [137]. Cao et al. studied the effect of TO at 700 °C for 5h in air on the tribocorrosion performance of Ti6Al4V and they revealed that the TO results in a hard multilayer oxide film that is constituted of a superficial oxide film below which an oxygen diffusion zone is present. The latter improves the tribocorrosion and the corrosion performance of the Ti alloy in 0.9 wt% NaCl solution [138]. It was also observed that the carburization of Ti6Al4V leads to the formation of nanocrystalline graphite that decreases the COF. Moreover, the carburized material shows a better tribocorrosion performance in simulated synovial fluid, however, the corrosion performance is deteriorated due to the uneven oxycarbide film formed. The incomplete formation of the oxycarbide layer may be attributed to the spatially inhomogenous carbon content present which suppresses the formation of TiO_2. Consequently, the material will actively corrode in the regions where the passive layer is hindered. It is worth mentioning that the biocompatibility of Ti6Al4V alloy is somehow maintained after carburization [114].

5.4 Laser Treatments

The use of laser treatments to functionalize metallic biomaterials is also discussed in the literature. The effect of laser remelting treatment on the tribocorrosion behavior of Ti6Al4V biomedical alloy was investigated in [139]. No difference was observed in the tribocorrosion behavior of the laser remelted and the untreated sample in extensive rubbing tribocorrosion tests. [139]. It was found that the laser cladding of Ti6Al4V alloy with cp-Ti ameliorates the tribocorrosion performance of the alloy in 3.5% NaCl solution. Hence, the dissolution of aluminum ions that can lead to neurological disorders is limited [120, 140]. This positive contribution of the treatment is more pronounced in 3.5% NaCl solutions with pH in the proximity of the neutral level [140]. The impact of the laser cladded $TiNiZrO_2$ composite coating on the tribocorrosion resistance of the Ti6Al4V alloy is also investigated in [151]. Another potential laser-based post-treatment to enhance the metallic bio-material tribocorrosion is laser shock peening. The latter ameliorates the tribocorrosion performance in 3.5 % NaCl of AZ31BMg alloy specifically at low laser power [141].

5.5 Mechanical Post Treatments

Mechanical post-treatments such as ultrasonic nanocrystal surface modification (UNSM), shot peening and surface mechanical attrition treatment (SMAT) have the potential of ameliorating the tribocorrosion performance of metallic biomaterials. UNSM modification can be employed to improve the tribocorrosion behavior of some biomedical alloys such as CoCrMo alloy. The UNSM illustrated in [109] was deployed on SLM-ed CoCrMo alloy at 25 °C and at 500 °C and it is witnessed that such treatments decrease the COF. It was also found that the UNSM achieved at high temperature somehow contributes more to the enhancement of the tribocorrosion properties of the material in 3.5% NaCl solution [109].

The tribocorrosion performance of AISI 4140 shot peened at distinct Almen intensity was studied in 3.5wt% NaCl solution. It was observed that the sample shot peened at the highest Almen intensity (24A) exhibits the best tribocorrosion performance [142]. Another possible mechanical post-treatment is surface mechanical attrition treatment (SMAT). After the latter, the grain boundary density increases. It is still controversial if this will lead to an enhancement in the material corrosion resistance. Nevertheless, this mechanical post-treatment augments the micro-hardness. Consequently, the wear resistance is ameliorated. Moreover, it induces compressive residual stresses at a higher depth than laser shock peening. In the latter, the compressive residual stress depth is limited by the plasma shock wave propagation distance. Sun et al. investigated the effect of SMAT on the tribocorrosion of 304 stainless steel in 0.9% NaCl solution. They observed that the SMAT reduces the COF. Moreover, it decreases the wear loss two to four times. This is attributed to the hardened layer formed after the SMAT [143].

6 Discussion

The AM processes are promising manufacturing techniques that can be utilized for the manufacturing of customized intricate hip implants. Nevertheless, until now, in the literature, most of the studies done on the tribocorrosion of AM-ed metallic biomaterials don't consider the complex infill structures deployed in the AM-ed femoral stem of the biomedical hip implant which is mainly affected by the tribocorrosion wear mechanism. The geometric factor that is not taken into account in the literature may play a pivotal role in inducing localized corrosion in the inner regions of the complex infill structure (e.g. gyroid infill or stochastic infill structures). This localized corrosion (i.e. cavitation or pitting corrosion) may be aggravated because it is difficult for the electrolyte present in the complicated infill structure to be refreshed. Therefore, the protons (H^+) resulting from the solvation of the metallic cations produced from the dissociation of the material will be concentrated in the solution. Therefore, the pH of the solution inside the infill structure will be relatively high. Consequently, the environment inside the infill structure becomes more aggressive and the destruction of the passive layer via localized corrosion or tribocorrosion is more facilitated. Thus, it is crucial to take into account the complex geometry of the AM-ed femoral stem. It is important to note that there exists no standard focusing on the procedure deployed to analyze the tribocorrosion of complex AM-ed metallic biomaterials. The majority of the tribocorrosion tests on AM-ed parts are done using a conventional 3-electrode system combined with a linear reciprocating tribometer. Such a setup does not take into consideration the geometrical effect of the implant as in hip simulators. The latter can help in mimicking scenarios close to the clinical situations. Almost all studies focusing on the tribocorrosion of metallic AM-ed parts discussed parts fabricated via the LENS or the SLM process. Nonetheless, non has studied the tribocorrosion of metallic biomaterials manufactured via indirect AM processes such as the metallic binder jetting process that has a relatively low production cost and is more commonly deployed in certain industries. The microstructures, the surface roughness and morphology, the porosity content and the mechanical and material properties of AM-ed metallic biomaterials are strongly dependent on the AM technique used. Typically, the tribocorrosion of AM-ed metallic biomaterials fabricated via direct energy techniques (i.e. SLM) may be affected by the strong microstructural texture and heterogeneity. Nonetheless, the

tribocorrosion of AM-ed materials manufactured via indirect processes such as metal fused filament deposition may be affected by the relatively high porosity content present in the vicinity of the analyzed surface. These porosities may act as micro-crevices at the open circuit potential. Thus, it can be seen that each AM-ed part processed via direct or indirect AM technique is characterized by specific microstructure and porosity content that may differ from that of the traditionally manufactured metallic biomaterials. Therefore, a sort of discrepancy may be found in the tribocorrosion properties between the AM-ed parts processed with distinct AM techniques and between the AM-ed metallic biomaterials and the conventionally fabricated parts. The role of third-body wear particles in the tribocorrosion wear mechanisms is still not extensively investigated in AM-ed metallic biomaterials. Moreover, the biological influence of such particulates and their interaction with their ambient biological environment are not studied. Regarding the tribocorrosion testing standards of metallic materials used in hip implants, even though the ASTMG119 and the UNE112086 provide a systematic approach for conducting in-vitro standard laboratory tribocorrosion tests, these standards still have some gaps and limitations that constraint the generalization of the tribocorrosion testing standards for the passivating and non passivating materials. It may be more critical to deeply understand the tribocorrosion mechanism than trying to compute the ASTMG119 synergy parameters that may have high errors. Furthermore, in Faraday's law, the computation of the corrosion wear Eq. 22 involves the number of electrons present in the material dissociation reactions. Nevertheless, there is no mere proof of which corrosion reactions are taking place during tribocorrosion [152]. It is also essential not to only simulate the mechanical conditions of the tribocorrosion test but also to apply the convenient biological and electrochemical conditions of the implant application like the ones proposed in [153]. There are several limitations or challenges confronted in the in-vitro testing of metallic materials for hip implants. It is difficult to measure in-situ the variation in the wear volume without stopping the test. Moreover, it is difficult to detect the local topographic, chemical and micro-structural changes taking place during the test. Unlike mechanical tests (i.e. tensile test or nanoindentation) it is almost impossible to do the tribocorrosion test in a scanning electron microscope (SEM) chamber. This makes it more difficult for researchers to accurately understand the tribocorrosion mechanism which may incorporate the interaction between several chemical, electrochemical, and mechanical processes.

Regarding the post-treatments applied to ameliorate the tribocorrosion of metallic biomaterials in hip implant application, few studies such as [106] have done post-treatments on AM-ed metallic biomaterials with a non-standard geometry. The main obstacle confronted in the post-treatment of AM-ed metallic biomaterials is achieving a homogeneous functionalization of the surface of the complex structure. Therefore, it is vital to choose a convenient post-treatment to functionalize the AM-ed metallic biomaterial. This is done based on the cost of the post-treatment, the material to be post-treated, the targeted resulting properties and the degree of the homogeneity of the post-treatment. For AM-ed metallic biomaterials, it may be better to deploy post-treatments in which the functionalization is done in a gas, liquid or plasma medium such as chemical vapor deposition, micro-arc oxidation or physical vapor deposition. Nonetheless, it may be required to change the orientation of the sample during the post-treatment.

Other post-treatments such as mechanical post-treatments may be challenging for intricate AM-ed metallic biomaterials. Mechanically post-treating complex thin infill structures used in hip implant applications may impose the risk of unfavorable dimensional modifications. The latter may result in the non-convenient fixation of the femoral stem to the bone. This leads to adverse consequences. Additionally, it is somehow difficult to uniformly deploy the UNSM, the shot peening or the SMAT on complex structures fabricated by AM. Furthermore, the balls used in shot peening and SMAT may be entrapped in the complex internal structure of the AM-ed femoral stem. It is important to note that in the literature, the effect of the post-treatments on the AM-ed metallic biomaterials is not meticulously studied. Based on the statistical analysis done on the studies (Fig. 16a), it can be seen that 70.58% of the addressed studies investigated post-treatments that can be properly deployed on intricate AM-ed parts. Nonetheless, the majority of the studies that investigate the post-treatments (88.57%) utilize a solution that doesn't contain any protein in their tribocorrosion tests (Fig. 16b). The proteins that are present in the human body may play a role in the bio-tribocorrosion process and in the biocorrosion mechanism ascribed to the interaction between corrosion and protein [154]. Variations in the corrosion and wear rate were observed due to the protein concentration [152]. Deeper multiscale comprehension of the bio-tribocorrosion mechanisms is essential to find appropriate post-treatments that can prohibit them. The tribocorrosion research can take advantage of the presence of in-situ characterization techniques that can enable the capturing of the local variations in temperature, electrolyte chemistry, wear, surface morphology and chemistry and mechanical properties. Techniques that may be used are in-situ-profilometry, in-situ-atomic force microscopy, in-situ-nanoindentation, Fourier transform infrared spectroscopy, and micro-Raman methods. The incorporation of such methods in the novel tribometers can aid in achieving a deeper understanding of the tribocorrosion and it avoids the sample contamination attributed to handling. Until now, the in-vitro tribocorrosion testing is not sufficient to fully certify a certain biomaterial

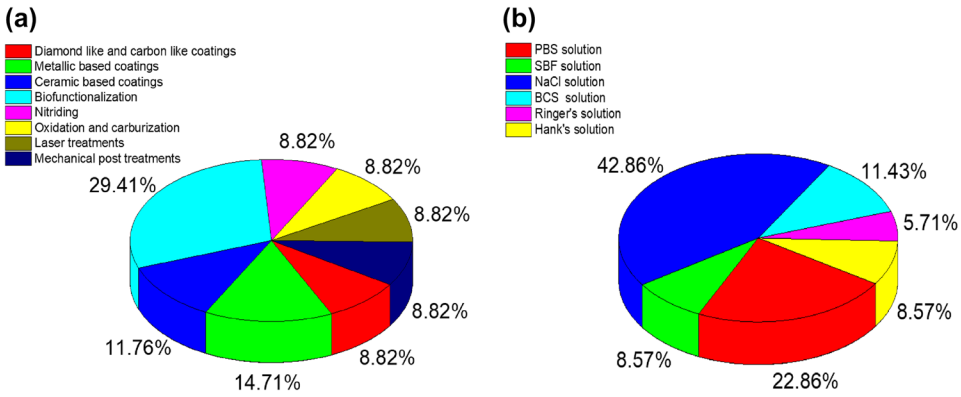

Fig. 16 Statistical analysis of the studies focusing on the potential post-treatments applied to ameliorate the tribocorrosion of metallic biomaterials in hip implant application. **b** The distribution of the studies based on the type of **a** post-treatments and **b** solutions

for use in hip implants in clinical situations. This is because it is difficult to simulate the intricate environment of the human body in which various types of cells, microorganisms and interconnected body organs and systems are present. It is important to note that the biological environment may have a time-dependent reaction to the tribocorrosion wear particles resulting from the tribocorrosion mechanism analyzed.

7 Conclusion

In conclusion, the available experimental techniques utilized to study the tribocorrosion of metallic biomaterials were discussed. Moreover, the state of art of tribocorrosion studies done on AM-ed metallic biomaterials utilized in hip implant applications was investigated. Finally, the potential post-treatments to ameliorate the tribocorrosion performance of hip implants AM-ed metallic biomaterials were shown.

OCP analysis, potentiostatic and potentiodynamic polarization and EIS can be deployed to analyze the tribocorrosion of metallic biomaterials. The two tribocorrosion experimental protocols were discussed to quantitatively asses the tribocorrosion wear and they are ASTMG119 and UNE112086. For the AM-ed metallic biomaterials, mainly the SLM-ed ones, anisotropy in the tribocorrosion and the corrosion behavior of the material is witnessed due to the heterogeneous microstructure. The potential post-treatments that can be deployed to ameliorate the tribocorrosion of hip implant metallic biomaterials can be classified into seven groups and they are: coatings, biofunctionalization, nitriding, oxidation, carburization, laser treatments and mechanical post treatments.

Coatings utilized to ameliorate the tribocorrosion performance of metallic biomaterials can be divided into Diamond like and carbon-based coatings, metallic materials based coatings and ceramic-based coatings. Biofunctionalization can be also deployed to various Ti alloys to enhance their biocompatibility and enhance the interaction between the implant material and the osteoblasts that are responsible for bone formation. Moreover, to the best of our knowledge, until now, only the study presented in [106] discussed the effect of biofunctionalization on the tribocorrosion of metallic AM-ed hip implant biomaterial. Nitriding, carburization and thermal oxidation yield the precipitation of hardening phases and the formation of protective layers that help in enhancing the material tribocorrosion. Laser cladding of metallic biomaterials such as cp-Ti can also have a favorable effect on the material tribocorrosion performance. Furthermore, mechanical peening treatments such as mechanical shock peening and SMAT augment the superficial hardness and induce compressive residual stresses to concurrently enhance the wear and corrosion resistance, respectively. Therefore, such treatments are promising to improve the metallic biomaterial tribocorrosion behavior in aggressive biological environments. Nonetheless, for AM-ed intricate structures, it is crucial to properly choose a post-treatment that can achieve a homogeneous functionalization of the material. Therefore, post-treatments in which the functionalization is done in a liquid, gaseous or plasma environment, where the deposition constituents can infiltrate the narrow geometrical voids of the complex AM-ed part, may be preferred.

Author Contributions This review was written by M. Naim who is supervised by A. Alhussein and M. Chemkhi. A. Alhussein and M. Chemkhi reviewed and edited this review article. Mahmoud NAIM: Conceptualization, Methodology, Formal analysis, Software, Writing—Original draft preparation. Akram ALHUSSEIN: Conceptualization, Resources, Writing—Reviewing and Editing, Supervision, Validation. Mahdi CHEMKHI: Conceptualization, Resources, Writing—Reviewing and Editing, Supervision, Validation.

Funding The authors gratefully acknowledge the financial support from the Regional Council of Champagne-Ardenne (France) through the CORR-FA project as well as from the EPF Graduate School of Engineering. They also acknowledge the FabAdd Platform of EPF Troyes for manufacturing the samples. The 'Troyes Champagne Métropole' and the Aube Department Council (France) are also acknowledged for their financial support of Markforged-Metal X System.

Availability of Data and Materials Not applicable.

Declarations

Competing Interest The authors declare that they have no conflicts of interest

Ethical Approval and Consent to Participate Not applicable

Consent for Publication Not applicable

References

1. Chemkhi M, Djouda JM, Bouaziz MA, Kauffmann J, Hild F, Retraint D (2021) Effects of mechanical post-treatments on additive manufactured 17–4ph stainless steel produced by bound powder extrusion. Procedia CIRP 104:957–961
2. Vunnam S, Saboo A, Sudbrack C, Starr TL (2019) Effect of powder chemical composition on the as-built microstructure of 17–4 ph stainless steel processed by selective laser melting. Addit Manuf 30:100876
3. Gratton A (2012) Comparison of mechanical, metallurgical properties of 17-4ph stainless steel between direct metal laser sintering (DMLs) and traditional manufacturing methods. 2012 NCUR
4. World's largest 3d metal printers (2022) https://www.relativityspace.com/stargate
5. Mutlu I, Oktay E (2013) Characterization of 17–4 ph stainless steel foam for biomedical applications in simulated body fluid and artificial saliva environments. Mater Sci Eng: C 33(3):1125–1131
6. Jevremović D, Kojić V, Bogdanović G, Puškar T, Eggbeer D, Thomas D, Williams R (2011) A selective laser melted Co-Cr alloy used for the rapid manufacture of removable partial denture frameworks: initial screening of biocompatibility. J Serbian Chem Soc 76(1):43–52
7. Ahangar P, Cooke ME, Weber MH, Rosenzweig DH (2019) Current biomedical applications of 3d printing and additive manufacturing. Appl Sci 9(8):1713
8. Jaisingh Sheoran Ankita, Kumar H, Arora PK, Moona G (2020) Bio-medical applications of additive manufacturing: a review. Procedia Manuf 51:663–670
9. Harun WSW, Manam NS, Kamariah MSIN, Sharif S, Zulkifly AH, Ahmad I, Miura H (2018) A review of powdered additive manufacturing techniques for ti-6al-4v biomedical applications. Powder Technol 331:74–97
10. Deng L, Wang S, Wang P, Kühn U, Pauly S (2018) Selective laser melting of a ti-based bulk metallic glass. Mater Lett 212:346–349
11. Zhang C, Li X, Liu S-Q, Liu H, Long-Jiang Y, Liu L (2019) 3d printing of Zr-based bulk metallic glasses and components for potential biomedical applications. J Alloys Compd 790:963–973
12. Fischer M, Laheurte P, Acquier P, Joguet D, Peltier L, Petithory T, Anselme K, Mille P (2017) Synthesis and characterization of Ti-27.5 Nb alloy made by clad® additive manufacturing process for biomedical applications. Mater Sci Eng: C 75:341–348
13. Attar H, Ehtemam-Haghighi S, Soro N, Kent D, Dargusch MS (2020) Additive manufacturing of low-cost porous titanium-based composites for biomedical applications: advantages, challenges and opinion for future development. J Alloys Compd 827:154263
14. Acharya S, Soni R, Suwas S, Chatterjee K (2021) Additive manufacturing of Co-Cr alloys for biomedical applications: a concise review. J Mater Res 36:3746–3760
15. Dadbakhsh S, Speirs M, Van Humbeeck J, Kruth J-P (2016) Laser additive manufacturing of bulk and porous shape-memory NiTi alloys: from processes to potential biomedical applications. MRS Bull 41(10):765–774
16. Lodhi MJK, Deen KM, Greenlee-Wacker MC, Haider W (2019) Additively manufactured 316l stainless steel with improved corrosion resistance and biological response for biomedical applications. Addit Manuf 27:8–19
17. Chehrehrazi S (2019) Influence of stress ratio on the torsional fatigue behaviour of 17-4PH stainless steel used for biomedical applications. PhD thesis, Wien
18. Parthasarathy J, Starly B, Raman S (2011) A design for the additive manufacture of functionally graded porous structures with tailored mechanical properties for biomedical applications. J Manuf Processes 13(2):160–170
19. Trevisan F, Calignano F, Aversa A, Marchese G, Lombardi M, Biamino S, Ugues D, Manfredi D (2018) Additive manufacturing of titanium alloys in the biomedical field: processes, properties and applications. J Appl Biomater Funct Mater 16(2):57–67
20. Cross MJ, Spycher J (2008) Cementless fixation techniques in joint replacement. Joint replacement technology. Elsevier, Amsterdam, pp 190–211
21. Capone A, Congia S, Civinini R, Marongiu G (2017) Periprosthetic fractures: epidemiology and current treatment. Clin Cases Miner Bone Metab 14(2):189
22. Huiskes R (1993) Stress shielding and bone resorption in THA: clinical versus computer-simulation studies. Acta Orthop Belg 59(Suppl 1):118–129
23. Hench L, Jones J (2005) Biomaterials, artificial organs and tissue engineering. Elsevier, Amsterdam
24. Hench LL (2005) 13-Joint replacement. In: Hench LL, Jones JR (eds) Biomaterials, artificial organs and tissue engineering. Woodhead Publishing Series in Biomaterials, Woodhead Publishing, pp 129–141
25. Huiskes R, Weinans H, Van Rietbergen B (1992) The relationship between stress shielding and bone resorption around total hip stems and the effects of flexible materials. Clin Orthop Relat Res 274:124–134
26. Shamieh LLD, Popa NM, Milodin NL, Gheorghiu D, Comsa S (2019) The importance of optimization of lattice structures for biomedical applications. Revista de Tehnologii Neconventionale 23(3):74–79
27. Eldesouky I, Harrysson O, West H, Elhofy H (2017) Electron beam melted scaffolds for orthopedic applications. Addit Manuf 17:169–175
28. Stendal J, Fergani O, Yamaguchi H, Espallargas N (2018) A comparative tribocorrosion study of additive manufactured and wrought 316l stainless steel in simulated body fluids. J Bio Tribo Corros 4(1):1–10
29. Ryu JJ, Shrotriya P (2013) Synergistic mechanisms of bio-tribocorrosion in medical implants. Bio-tribocorrosion in biomaterials and medical implants. Elsevier, Amsterdam, pp 25–44
30. Akdogan G (2019) Corrosion residue debris left by implant materials to the patient's body. Am J Biomed Sci Res 6(3):176–178
31. Total hip replacement-orthoinfo-aaos. https://orthoinfo.aaos.org/en/treatment/total-hip-replacement
32. Kurtz S, Ong K, Lau E, Mowat F, Halpern M (2007) Projections of primary and revision hip and knee arthroplasty in the united states from 2005 to 2030. JBJS 89(4):780–785
33. Ødegaard KS, Torgersen J, Elverum CW (2020) Structural and biomedical properties of common additively manufactured biomaterials: a concise review. Metals 10(12):1677

34. Gill IPS, Webb J, Sloan K, Beaver RJ (2012) Corrosion at the neck-stem junction as a cause of metal ion release and pseudotumour formation. J Bone Joint Surg Br 94(7):895–900
35. Shittu J, Sadeghilaridjani M, Pole M, Muskeri S, Ren J, Liu Y, Tahoun I, Arora H, Chen W, Dahotre N et al (2021) Tribo-corrosion response of additively manufactured high-entropy alloy. NPJ Mater Degrad 5(1):1–8
36. Mathew MT, Srinivasa PP, Pourzal R, Fischer A, Wimmer MA (2009) Significance of tribocorrosion in biomedical applications: overview and current status. Adv Tribol. https://doi.org/10.1155/2009/250986
37. Wood Robert JK (2007) Tribo-corrosion of coatings: a review. J Phys D: Appl Phys 40(18):5502
38. Taufiqurrakhman M, Neville A, Bryant MG (2021) The effect of protein structure and concentration on tribocorrosion and film formation on cocrmo alloys. J Bio Tribo Corros 7:1–18
39. Buciumeanu M, Bagheri A, Shamsaei N, Thompson SM, Silva FS, Henriques B (2018) Tribocorrosion behavior of additive manufactured Ti-6Al-4V biomedical alloy. Tribol Int 119:381–388
40. Yan Y, Neville A (2013) Bio-tribocorrosion: surface interactions in total joint replacement (TJR). Bio-tribocorrosion in biomaterials and medical implants. Elsevier, Amsterdam, pp 309–340
41. Zhao G-H, Aune RE, Espallargas N (2016) Tribocorrosion studies of metallic biomaterials: the effect of plasma nitriding and DLC surface modifications. J Mech Behav Biomed Mater 63:100–114
42. Malik A, Rouf S, Haq MIU, Raina A, Puerta APV, Sagbas B, Ruggiero A (2022) Tribo-corrosive behavior of additive manufactured parts for orthopaedic applications. J Orthop 34:49–60
43. Sipek KT, Lyvers ME, Mathew MT (2018) Failure causes in total hip replacements: a review. Austin J Orthop Rheumatol 5:1064
44. Schaaff P (2004) The role of fretting damage in total hip arthroplasty with modular design hip joints-evaluation of retrieval studies and experimental simulation methods. J Appl Biomater Biomech 2(3):121–135
45. Vingsbo O, Söderberg S (1988) On fretting maps. Wear 126(2):131–147
46. Vantadori S, Vázquez VJ, Zanichelli A, Carpinteri A, Luciano R (2022) Structural integrity of shot peened Ti6Al4V specimens under fretting fatigue. Int J Fract 234(1–2):45–55
47. Oladokun A, Pettersson M, Bryant M, Engqvist H, Persson C, Hall R, Neville A (2015) Fretting of cocrmo and ti6al4v alloys in modular prostheses. Tribol Mater Surf Interfaces 9(4):165–173
48. Neu RW (2011) Progress in standardization of fretting fatigue terminology and testing. Tribol Int 44(11):1371–1377
49. Costa AI, Viana F, Toptan F, Geringer J (2021) Highly porous Ti as a bone substitute: triboelectrochemical characterization of highly porous Ti against Ti alloy under fretting-corrosion conditions. Corros Sci 190:109696
50. Semetse L, Obadele BA, Raganya L, Geringer J, Olubambi PA (2019) Fretting corrosion behaviour of Ti-6Al-4V reinforced with zirconia in foetal bovine serum. J Mech Behav Biomed Mater 100:103392
51. Feyzi M, Fallahnezhad K, Taylor M, Hashemi R (2022) An overview of the stability and fretting corrosion of microgrooved necks in the taper junction of hip implants. Materials 15(23):8396
52. Gilbert JL, Buckley CA, Jacobs JJ (1993) In vivo corrosion of modular hip prosthesis components in mixed and similar metal combinations. The effect of crevice stress motion and alloy coupling. J Biomed Mater Res 27(12):1533–1544
53. Bryant M (2013) Fretting-crevice corrosion of cemented metal on metal total hip replacements. University of Leeds, Leeds
54. Hallab NJ, Messina S, Skipor A, Jacobs JJ (2004) Differences in the fretting corrosion of metal-metal and ceramic-metal modular junctions of total hip replacements. J Orthop Res 22(2):250–259
55. Zajc J, Fokter SK (2022) Dual-modular stems for primary total hip arthroplasty. Encyclopedia 2(2):893–911
56. Sin JR (2015) Investigation of the corrosion and tribocorrosion behaviour of metallic biomaterials. PhD thesis, Luleå tekniska universitet
57. Sidaginamale RP, Joyce TJ, Bowsher JG, Lord JK, Avery PJ, Natu S, Nargol AVF, Langton DJ (2016) The clinical implications of metal debris release from the taper junctions and bearing surfaces of metal-on-metal hip arthroplasty: joint fluid and blood metal ion concentrations. Bone Joint J 98(7):925–933
58. Liang Y, Ma M, Zhang F, Liu F, Lu T, Liu Z, Li Y (2021) Wireless microfluidic sensor for metal ion detection in water. ACS Omega 6(13):9302–9309
59. Shittu J, Pole M, Cockerill I, Sadeghilaridjani M, Reddy LVK, Manivasagam G, Singh H, Grewal HS, Arora HS, Mukherjee S (2020) Biocompatible high entropy alloys with excellent degradation resistance in a simulated physiological environment. ACS Appl Bio Mater 3(12):8890–8900
60. Alnajjar M (2019) Corrosion properties of 17-4 PH martensitic stainless steel obtained by additive manufacturing. PhD thesis, Lyon
61. Huang W, Wang Z, Liu C, Yongmei Y (2015) Wear and electrochemical corrosion behavior of biomedical Ti-25Nb-3Mo-3Zr-2Sn alloy in simulated physiological solutions. J Bio Tribo Corros 1(1):1–10
62. Wang L, Snihirova D, Deng M, Vaghefinazari B, Höche D, Lamaka SV, Zheludkevich ML (2022) Revealing physical interpretation of time constants in electrochemical impedance spectra of mg via tribo-eis measurements. Electrochim Acta 404:139582
63. Basics of electrochemical impedance spectroscopy. https://www.gamry.com/application-notes/EIS/basics-of-electrochemical-impedance-spectroscopy/
64. Magar HS, Hassan RYA, Mulchandani A (2021) Electrochemical impedance spectroscopy (eis): Principles, construction, and biosensing applications. Sensors 21(19):6578
65. What is electrochemical impedance spectroscopy (eis)? (electrochemistry basics series). https://www.biologic.net/topics/what-is-eis/, Jun (2022)
66. Nikitas D, Celis J-P, Pierre P, François W (2009) A methodology for the assessment of the tribocorrosion of passivating metallic materials. Lubr Sci 21(2):53–67
67. López A, Bayón R, Pagano F, Igartua A, Arredondo A, Arana JL, González JJ (2015) Tribocorrosion behaviour of mooring high strength low alloy steels in synthetic seawater. Wear 338:1–10
68. Standard guide for determining synergism between wear and corrosion. https://www.astm.org/g0119-09r21.html
69. Stack MM, Rodling J, Mathew MT, Jawan H, Huang W, Park G, Hodge C (2010) Micro-abrasion-corrosion of a co-cr/uhmwpe couple in ringer's solution: an approach to construction of mechanism and synergism maps for application to bio-implants. Wear 269(5–6):376–382
70. Calculation of corrosion rate (2022) https://www.gamry.com/Framework%20Help/HTML5%20-%20Tripane%20-%20Audience%20A/Content/EFM/Introduction/Calculation%20of%20Corrosion%20Rate.htm
71. Electrochemical kinetics of corrosion (2022) https://www.uobabylon.edu.iq/eprints/publication_12_18564_228.pdf
72. Fuentes E, Alves S, López-Ortega A, Mendizabal L, de Viteri VS (2019) Advanced surface treatments on titanium and titanium alloys focused on electrochemical and physical technologies for biomedical applications. Biomaterial-supported tissue reconstruction or regeneration

73. Zhang Y, Yin X, Wang J, Yan F (2014) Influence of microstructure evolution on tribocorrosion of 304ss in artificial seawater. Corros Sci 88:423–433
74. López-Ortega A, Arana JL, Bayón R (2018) Tribocorrosion of passive materials: a review on test procedures and standards. Int J Corros 2018
75. Xue Y, Yi H, Wang Z (2019) Tribocorrosion behavior of NiTi alloy as orthopedic implants in ringer's simulated body fluid. Biomed Phys Eng Express 5(4):045002
76. Wang Z, Huang W, Li Y, He H, Zhou Y, Zheng Z (2017) Tribocorrosion behaviour of a biomedical Ti-25Nb-3Mo-3Zr-2Sn alloy in ringer's solution. Mater Sci Eng: C 76:1094–1102
77. Licausi MP, Igual Muñoz A, Amigó Borrás V (2013) Influence of the fabrication process and fluoride content on the tribocorrosion behaviour of Ti6Al4V biomedical alloy in artificial saliva. J Mech Behav Biomed Mater 20:137–148
78. Xin L, Zhang D, Wei X, Aihua Y, Zhang J, Tamaddon M, Zhang J, Xuanhui Q, Liu C, Bo S (2020) The effect of cu content on corrosion, wear and tribocorrosion resistance of Ti-Mo-Cu alloy for load-bearing bone implants. Corros Sci 177:109007
79. Neto MQ, Rainforth WM (2021) Effect of potential and microstructure on the tribocorrosion behaviour of beta and near beta Ti alloys II. J Bio Tribo Corros 7(4):1–12
80. Farooqui MS (2017) An electrochemical and tribocorrosion study on austenitic high nitrogen steel in orthopedic applications. PhD thesis, University of Illinois at Chicago
81. Ferreira DF, Almeida SMA, Soares RB, Juliani L, Bracarense AQ, Lins VDFC, Junqueira RMR (2019) Synergism between mechanical wear and corrosion on tribocorrosion of a titanium alloy in a ringer solution. J Mater Res Technol 8(2):1593–1600
82. Sharma N, Singh G, Hegab H, Mia M, Batra NK (2019) Tribocorrosion characterization of NiTiCu alloy for bio-implant applications. Mater Res Express 6(9):096526
83. More NS, Diomidis N, Paul SN, Roy M, Mischler S (2011) Tribocorrosion behavior of β titanium alloys in physiological solutions containing synovial components. Mater Sci Eng: C 31(2):400–408
84. Chávez J, Jimenez O, Olmos L, Farias I, Flores-Jimenez M, Suárez-Martínez R, Cabezas-Villa JL, Lemus-Ruiz J (2020) Tribocorrosion behavior of Ti64-xta alloys fabricated through powder metallurgy. Mater Lett 280:128590
85. Borrás AD, Buch AR, Cardete AR, Navarro-Laboulais J, Munoz AI (2019) Chemo-mechanical effects on the tribocorrosion behavior of titanium/ceramic dental implant pairs in artificial saliva. Wear 426:162–170
86. Radice S, Neto MQ, Fischer A, Wimmer MA (2021) Nickel-free high-nitrogen austenitic steel outperforms cocrmo alloy regarding tribocorrosion in simulated inflammatory synovial fluids. J Orthop Res®
87. Sousa L, Alves AC, Guedes A, Toptan F (2021) Corrosion and tribocorrosion behaviour of Ti-B4C composites processed by conventional sintering and hot-pressing technique. J Alloys Compd 885:161109
88. Correa DRN, Kuroda PAB, Grandini CR, Rocha LA, Oliveira FGM, Alves AC, Toptan F (2016) Tribocorrosion behavior of β -type ti-15zr-based alloys. Mater Lett 179:118–121
89. Pina VG, Dalmau A, Devesa F, Amigó V, Muñoz AI (2015) Tribocorrosion behavior of beta titanium biomedical alloys in phosphate buffer saline solution. J Mech Behav Biomed Mater 46:59–68
90. Espallargas N, Aune RE, Torres C, Papageorgiou N, Muñoz AI (2013) Bulk metallic glasses (BMG) for biomedical applications-a tribocorrosion investigation of Zr55Cu30Ni5Al10 in simulated body fluid. Wear 301(1–2):271–279
91. Doni Z, Alves AC, Toptan F, Pinto AM, Rocha LA, Buciumeanu M, Palaghian L, Silva FS (2014) Tribocorrosion behaviour of hot pressed cocrmo- Al2O3 composites for biomedical applications. Tribol Mater Surf Interfaces 8(4):201–208
92. Kosec T, Močnik P, Legat A (2014) The tribocorrosion behaviour of NiTi alloy. Appl Surf Sci 288:727–735
93. Shivaram MJ, Arya SB, Nayak J, Panigrahi BB (2021) Tribocorrosion behaviour of biomedical porous Ti-20Nb-5Ag alloy in simulated body fluid. J Bio Tribo Corros 7(2):1–9
94. Runa MJ, Mathew MT, Rocha LA (2013) Tribocorrosion response of the ti6al4v alloys commonly used in femoral stems. Tribol Int 68:85–93
95. Buciumeanu M, Araujo A, Carvalho O, Miranda G, Souza JCM, Silva FS, Henriques B (2017) Study of the tribocorrosion behaviour of Ti6Al4V-ha biocomposites. Tribol Int 107:77–84
96. Hua N, Chen W, Wang Q, Guo Q, Huang Y, Zhang T (2018) Tribocorrosion behaviors of a biodegradable Mg65Zn30Ca5 bulk metallic glass for potential biomedical implant applications. J Alloys Compd 745:111–120
97. Doni Z, Alves AC, Toptan F, Gomes JR, Ramalho A, Buciumeanu M, Palaghian L, Silva FS (2013) Dry sliding and tribocorrosion behaviour of hot pressed cocrmo biomedical alloy as compared with the cast cocrmo and Ti6Al4V alloys. Mater Des 1980–2015(52):47–57
98. Caha I, Alves AC, Kuroda PAB, Grandini CR, Pinto AMP, Rocha LA, Toptan F (2020) Degradation behavior of Ti-Nb alloys: Corrosion behavior through 21 days of immersion and tribocorrosion behavior against alumina. Corros Sci 167:108488
99. Hacisalihoglu I, Samancioglu A, Yildiz F, Purcek G, Alsaran A (2015) Tribocorrosion properties of different type titanium alloys in simulated body fluid. Wear 332:679–686
100. Licausi M-P, Muñoz AI, Borrás VA (2013) Tribocorrosion mechanisms of Ti6Al4V biomedical alloys in artificial saliva with different pHs. J Phys D: Appl Phys 46(40):404003
101. Çaha I, Alves A, Chirico C, Pinto A, Tsipas S, Gordo E, Toptan F (2020) Corrosion and tribocorrosion behavior of Ti-40Nb and Ti-25Nb-5Fe alloys processed by powder metallurgy. Metall Mater Trans A 51(6):3256–3267
102. Vilhena L, Oppong G, Ramalho A (2019) Tribocorrosion of different biomaterials under reciprocating sliding conditions in artificial saliva. Lubr Sci 31(8):364–380
103. Henry P, Takadoum J (2009) Friction and tribocorrosion of 316l stainless steel against uhmwpe or alumina in saline solution. Tribol Mater Surf Interfaces 3(2):84–91
104. Toptan F, Alves AC, Carvalho Ó, Bartolomeu F, Pinto AMP, Silva F, Miranda G (2019) Corrosion and tribocorrosion behaviour of Ti6Al4V produced by selective laser melting and hot pressing in comparison with the commercial alloy. J Mater Process Technol 266:239–245
105. Chiu T-M, Mahmoudi M, Dai W, Elwany A, Liang H, Castaneda H (2018) Corrosion assessment of Ti-6Al-4V fabricated using laser powder-bed fusion additive manufacturing. Electrochim Acta 279:143–151
106. Bartolomeu F, Buciumeanu M, Costa MM, Alves N, Gasik M, Silva FS, Miranda G (2019) Multi-material Ti6Al4V & peek cellular structures produced by selective laser melting and hot pressing: a tribocorrosion study targeting orthopedic applications. J Mech Behav Biomed Mater 89:54–64
107. Avila JD, Alrawahi Z, Bose S, Bandyopadhyay A (2020) Additively manufactured Ti6Al4V-Si-hydroxyapatite composites for articulating surfaces of load-bearing implants. Addit Manuf 34:101241
108. Chen J, Li C, Zhou L, Ren Y, Li C, Liao X, Wang Y, Niu Y (2022) The anisotropic of corrosion and tribocorrosion behaviors

of Ti15Mo alloy fabricated by selective laser melting. Mater Charact 190:112000
109. Amanov A (2021) Effect of post-additive manufacturing surface modification temperature on the tribological and tribocorrosion properties of Co-Cr-Mo alloy for biomedical applications. Surf Coat Technol 421:127378
110. Dai N, Zhang LC, Zhang J, Zhang X, Ni Q, Chen Y, Wu M, Yang C (2016) Distinction in corrosion resistance of selective laser melted Ti-6Al-4V alloy on different planes. Corros Sci 111:703–710
111. Liu Y, Mace A, Lee H, Camargo M, Gilbert JL (2022) Single asperity sub-nano to nanoscale wear and tribocorrosion of wrought CoCrMo and additively manufactured cocrmow alloys. Tribol Int 174:107770
112. Grabarczyk J, Gaj J, Pazik B, Kaczorowski W, Januszewicz B (2021) Tribocorrosion behavior of Ti6Al4V alloy after thermochemical treatment and DLC deposition for biomedical applications. Tribol Int 153:106560
113. Azzi M, Paquette M, Szpunar JA, Klemberg-Sapieha JE, Martinu L (2009) Tribocorrosion behaviour of DLC-coated 316l stainless steel. Wear 267(5–8):860–866
114. Cheng K-Y, Pagan N, Bijukumar D, Mathew MT, McNallan M (2018) Carburized titanium as a solid lubricant on hip implants: corrosion, tribocorrosion and biocompatibility aspects. Thin Solid Films 665:148–158
115. Cheng K-Y, Nargaraj R, Bijukumar D, Mathew MT, McNallan M (2020) Improvement of tribocorrosion behavior on titanium alloy by carbide-derived carbon (CDC). Surf Coat Technol 392:125692
116. Beliardouh NE, Ramoul CE, Nouveau C, Kaleli EH, Montagne A (2022) Synthesis and tribocorrosion performances of multilayer (Ta/ZrN) n coatings. Thin Solid Films 749:139184
117. Chen SN, Zhao YM, Zhang YF, Chen L, Liao B, Zhang X, Ouyang XP (2021) Influence of carbon content on the structure and tribocorrosion properties of TiAlCN/TiAlN/TiAl multilayer composite coatings. Surf Coat Technol 411:126886
118. Alemón B, Flores M, Ramírez W, Huegel JC, Broitman E (2015) Tribocorrosion behavior and ions release of CoCrMo alloy coated with a TiAlvCN/CNx multilayer in simulated body fluid plus bovine serum albumin. Tribol Int 81:159–168
119. Ureña J, Tsipas S, Pinto AM, Toptan F, Gordo E, Jiménez-Morales A (2018) Corrosion and tribocorrosion behaviour of β-type Ti-Nb and Ti-Mo surfaces designed by diffusion treatments for biomedical applications. Corros Sci 140:51–60
120. Hee AC, Martin PJ, Bendavid A, Jamali SS, Zhao Y (2018) Tribo-corrosion performance of filtered-arc-deposited tantalum coatings on Ti-13Nb-13Zr alloy for bio-implants applications. Wear 400:31–42
121. Cheng K-Y, Gopal V, McNallan M, Manivasagam G, Mathew MT (2019) Enhanced tribocorrosion resistance of hard ceramic coated Ti-6Al-4V alloy for hip implant application: in-vitro simulation study. ACS Biomater Sci Eng 5(9):4817–4824
122. Gao Z, Ji G, Shi Z, Wang X (2021) The tribocorrosion behaviour of ysz coating deposited on stainless steel substrate in 3.5 wt% nacl solution. Ceram Int 47(15):21051-21060
123. Sourani F, Raeissi K, Enayati MH, Kharaziha M, Hakimizad A, Salimijazi HR (2022) Corrosion and tribocorrosion behavior of ZrO2-Al2O3 composite coatings developed by plasma electrolytic oxidation for load-bearing implants. SSRN 4045433
124. Pana I, Vladescu A, Constantin LR, Sandu IG, Dinu M, Cotrut CM (2020) In vitro corrosion and tribocorrosion performance of biocompatible carbide coatings. Coatings 10(7):654
125. Fazel M, Salimijazi HR, Golozar MA et al (2015) A comparison of corrosion, tribocorrosion and electrochemical impedance properties of pure ti and ti6al4v alloy treated by micro-arc oxidation process. Appl Surf Sci 324:751–756
126. Sousa L, Basilio L, Alves AC, Toptan F (2021) Tribocorrosion-resistant biofunctionalized Ti-Al2O3 composites. Surf Coat Technol 420:127329
127. Alves AC, Oliveira F, Wenger F, Ponthiaux P, Celis J-P, Rocha LA (2013) Tribocorrosion behaviour of anodic treated titanium surfaces intended for dental implants. J Phys D: Appl Phys 46(40):404001
128. Zuo Y, Li T, Jiang X, Wu M, Zhang Y, Chen F (2020) Tribocorrosion behavior of ca-p mao coatings on ti6al4v alloy at various applied voltages. J Mater Res 35(5):444–453
129. Laurindo CAH, Bemben LM, Torres RD, Mali SA, Gilbert JL, Soares P (2016) Influence of the annealing treatment on the tribocorrosion properties of ca and p containing TiO2 produced by plasma electrolytic oxidation. Mater Technol 31(12):719–725
130. Fazel M, Shamanian M, Salimijazi HR (2020) Enhanced corrosion and tribocorrosion behavior of Ti6Al4V alloy by auto-sealed micro-arc oxidation layers. Biotribology 23:100131
131. Lee C-K (2012) Fabrication, characterization and wear corrosion testing of bioactive hydroxyapatite/nano-TiO2 composite coatings on anodic Ti-6Al-4V substrate for biomedical applications. Mater Sci Eng: B 177(11):810–818
132. Çaha I, Alves AC, Chirico C, Pinto AMP, Tsipas S, Gordo E, Toptan F (2021) A promising method to develop TiO2-based nanotubular surfaces on Ti-40Nb alloy with enhanced adhesion and improved tribocorrosion resistance. Appl Surf Sci 542:148658
133. Çaha I, Alves AC, Chirico C, Pinto AM, Tsipas S, Gordo E, Toptan F (2021) Improved tribocorrosion behavior on bio-functionalized β-type titanium alloy by the pillar effect given by tin reinforcements. Surf Coat Technol 415:127122
134. Albayrak Ç, Hacısalihoğlu İ, Alsaran A et al (2013) Tribocorrosion behavior of duplex treated pure titanium in simulated body fluid. Wear 302(1–2):1642–1648
135. Çaha I, Alves AC, Affonço LJ, da Silva JHD, Rodrigues IR, Grandini CR, Rocha LA, Pinto AMP, Lisboa-Filho PN, Toptan F (2021) Degradation behaviour of Ti-12Nb alloy coated with ZnO/tin double layer. Surf Coat Technol 413:127104
136. Guan J, Jiang X, Xiang Q, Yang F, Liu J (2021) Corrosion and tribocorrosion behavior of titanium surfaces designed by electromagnetic induction nitriding for biomedical applications. Surf Coat Technol 409:126844
137. Bailey R (2018) Tribocorrosion response of surface-modified Ti in a 0.9% NaCl solution. Lubricants 6(4):86
138. Cao L, Wan Y, Yang S, Pu J (2018) The tribocorrosion and corrosion properties of thermally oxidized Ti6Al4V alloy in 0.9 wt.% NaCl physiological saline. Coatings 8(8):285
139. Silva DP, Churiaque C, Bastos IN, Sánchez-Amaya JM (2016) Tribocorrosion study of ordinary and laser-melted Ti6Al4V alloy. Metals 6(10):253
140. Obadele BA, Andrews A, Olubambi PA, Mathew MT, Pityana S (2015) Tribocorrosion behaviour of laser cladded biomedical grade titanium alloy. Mater Corros 66(10):1133–1139
141. Siddaiah A, Mao B, Liao Y, Menezes PL (2020) Effect of laser shock peening on the wear-corrosion synergistic behavior of an az31b magnesium alloy. J Tribol 142(4):041701
142. Bozkurt YB, Kovacı H, Yetim AF, Çelik A (2022) Tribocorrosion properties and mechanism of a shot peened AISI 4140 low-alloy steel. Surf Coat Technol 440:128444
143. Sun Y, Bailey R (2014) Improvement in tribocorrosion behavior of 304 stainless steel by surface mechanical attrition treatment. Surf Coat Technol 253:284–291
144. Roy RK, Lee K-R (2007) Biomedical applications of diamond-like carbon coatings: a review. J Biomed Mater Res Part B: Appl Biomater 83(1):72–84

145. Allen M, Myer B, Rushton N (2001) In vitro and in vivo investigations into the biocompatibility of diamond-like carbon (DLC) coatings for orthopedic applications. J Biomed Mater Res 58(3):319–328
146. Caetano-Lopes J, Canhao H, Fonseca JE (2007) Osteoblasts and bone formation. Acta reumatológica portuguesa 32(2):103–110
147. Alves SA, Rossi AL, Ribeiro AR, Toptan F, Pinto AM, Shokuhfar T, Celis J-P, Rocha LA (2018) Improved tribocorrosion performance of bio-functionalized TiO2 nanotubes under two-cycle sliding actions in artificial saliva. J Mech Behav Biomed Mater 80:143–154
148. Alves SA, Bayón R, de Viteri VS, Garcia MP, Igartua A, Fernandes MH, Rocha LA (2015) Tribocorrosion behavior of calcium-and phosphorous-enriched titanium oxide films and study of osteoblast interactions for dental implants. J Bio Tribo Corros 1(3):1–21
149. Zuo Y, Li T, Yu P, Zhao Z, Chen X, Zhang Y, Chen F (2019) Effect of graphene oxide additive on tribocorrosion behavior of MAO coatings prepared on Ti6Al4V alloy. Appl Surf Sci 480:26–34
150. Souza JCM, Tajiri HA, Morsch CS, Buciumeanu M, Mathew MT, Silva FS, Henriques B (2015) Tribocorrosion behavior of Ti6Al4V coated with a bio-absorbable polymer for biomedical applications. J Bio Tribo Corros 1(4):1–6
151. Obadele BA, Andrews A, Mathew MT, Olubambi PA, Pityana S (2015) Improving the tribocorrosion resistance of Ti6Al4V surface by laser surface cladding with TiNiZrO2 composite coating. Appl Surf Sci 345:99–108
152. Blau P, Stack M, Wood R, Mischler S, Jiang J, Drees D, Rocha L, Wimmer M, Celis J-P, Cowan R (2013) Future needs for tribocorrosion research and testing
153. Rosenbloom SN, Corbett RA (2007) An assessment of astm f 2129 electrochemical testing of small medical implants-lessons learned. In: CORROSION 2007. OnePetro
154. Talha M, Ma Y, Kumar P, Lin Y, Singh A (2019) Role of protein adsorption in the bio corrosion of metallic implants-a review. Colloids Surf B: Biointerfaces 176:494–506